3-31-2023

Improved Selectivity and Stability in Methane Dry Reforming by Atomic Layer Deposition onto Ni-CeO2-ZrO2/Al2O3 Catalysts

Jonathan Lucas
Louisiana State University and Agricultural and Mechanical College

IMPROVED SELECTIVITY AND STABILITY IN METHANE DRY REFORMING BY ATOMIC LAYER DEPOSITION ONTO Ni-CeO_2-ZrO_2/Al_2O_3 CATALYSTS

A Thesis

Submitted to the Graduate Faculty of the
Louisiana State University and
Agriculture and Mechanical College
in partial fulfillment of the
requirements for the degree of
Master of Science

in

The Cain Department of Chemical Engineering

by
Jonathan Lucas
B.S., Louisiana State University, 2020
May 2023

Table of Contents

List of Tables

List of Figures

Abstract

The use of Ni in the dry reforming of methane (DRM) has been widely studied as a replacement for noble metal catalysts (Pt, Pd, Rh) due to Ni's low cost compared to noble metals, its abundance, and the fact that its DRM activity is near that of noble metal catalysts. However, Ni has been shown to deactivate quickly under DRM conditions. Rare earth oxides such as CeO_2, or as CeO_2-ZrO_2 (CZO) are supports that improve both the activity and stability of Ni DRM systems due to their redox activity. However, this same activity is thought to enhance the undesired reverse water gas shift (RWGS) reaction, reducing the hydrogen selectivity. In this work, Ni:CZA nanoparticles were coated with an Al_2O_3 overlayer using an atomic layer deposition (ALD) method to study the effect an Al_2O_3 overlayer would have on the catalysts: their activity, stability, and H_2/CO ratio, when compared to an uncoated reference. A low conversion screening method showed an improvement in DRM activity and coking rate upon the addition of an Al_2O_3 ALD overcoat, and this improvement was also seen in a higher conversion lab scale reactor. The overcoated sample displayed an ~1 H_2/CO ratio in the high conversion reactor. Analysis of X-ray absorption spectroscopy (XAS) and X-ray photoelectron spectroscopy (XPS) showed that the active Ni oxidation state was +2 and that Ni-Ce-Al were most likely present as mixed oxides in the overlayer level of the structure.

Chapter 1. Introduction

1.1. Motivation

Both the US and EU have placed significant importance on reducing emitted greenhouse gases (GHGs) to achieve no more than a 2°C increase in atmospheric temperature and mitigate the worst of the expected climate disasters due to climate warming. To achieve this goal, one study by Liu et al. explains that the US alone needs to increase the reduction of CO_2 by 38% greater than their nationally determined contributions of a 52% reduction in CO_2 emission compared to 2005 levels, that was agreed upon at the 2015 Paris Agreement.[1] Furthermore, comparisons of the US emissions to the EU, China, and India show that significant effort is needed to achieve just the half-decade (2025) emission goal of 5000 Mt CO_2 emitted per year, as shown in Figure 1.1.[2]

Therefore, chemical transformation of CO_2 have been widely studied, as a way to reduce greenhouse gases through a more carbon-neutral petrochemical industry.[3, 4] Due to the high stability of the CO_2 molecule, chemical transformation is usually achieved through catalytic processes such as the dry reforming of methane (DRM), hydrogenation, formation of carbonate species, etc.[5-7] DRM has been widely studied due to the potential to transform the two major greenhouse gases CH_4 and CO_2, into syngas (H_2, CO) at close to a 1:1 ratio this would need to be adjusted for follow up processes such as Fischer Tropsch.[8]

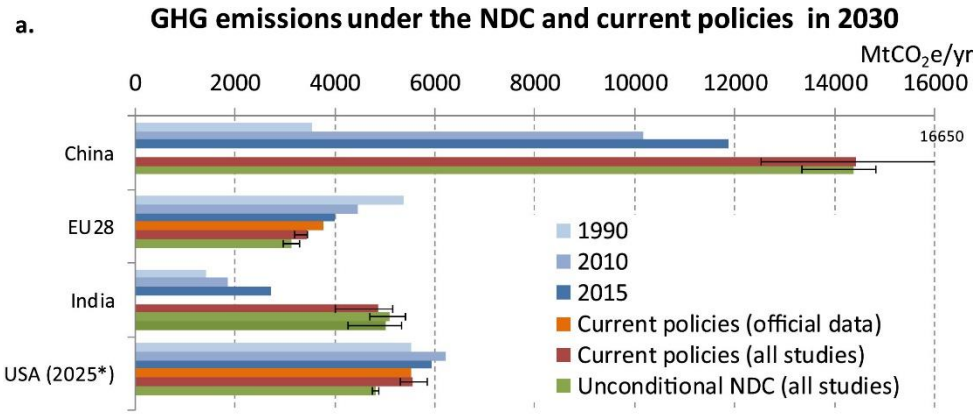

Figure 1

Figure 1.1. GHG of G20 members in the target year (2030), US (2025).[2]

Due to the slow kinetics of DRM (eq1.1), the reaction is typically done at temperatures exceeding 700°C, which leads to stability issues such as sintering of the active metal.[9-11]In addition, coke-forming reactions are present during DRM, such as the Boudouard (eq 1.2) and methane decomposition (eq 1.3) reactions. Along with these deactivation mechanisms, DRM is affected by the reverse water gas shift (RWGS, eq 1.4) reaction, lowering the H_2/CO ratio.

$$CH_4 + CO_2 \rightarrow 2H_2 + 2CO \qquad (1.1)$$

$$2CO \leftrightarrow C(s) + CO_2 \qquad (1.2)$$

$$CH_4 \rightarrow 2H_2 + C(s) \qquad (1.3)$$

$$CO_2 + H_2 \rightarrow H_2O + CO \qquad (1.4)$$

Lowering the reaction temperature to diminish the aggregation of the active metal particles enhances competition from the RWGS and Boudouard reactions, both of which are more favorable thermodynamically at <700°C. If equilibrium is assumed for both RWGS and DRM (calculations with Aspen Plus®), the equilibrium H_2/CO ratio decreases from 0.86 to 0.80 for 700

→ 650 °C. If equilibrium is assumed for all three reactions, the amount of amorphous coke per mol CH4 fed increases from 0.29 to 040 for 700 → 650 °C.[12]

Ni-based DRM catalysts have seen increased attention over the past few decades due to their economic advantage over noble metal catalysts (Pt, Pd, Rh), and promising catalytic performance.[13-15] However, Ni is highly susceptible to the deactivation mechanisms of coking and sintering. Due to the low Tammann temperature (700°C, the temperature at which atoms in the crystal lattice become mobile) of Ni, sintering and the loss of active surface area is a significant issue in Ni-based DRM. Aggregation of Ni particles also leads to enhanced coking.[9, 10, 16, 17] Therefore, suppression of sintering is the most important problem to be solved to enable use of Ni-based DRM catalysts on a large scale.

To maximize the conversion of DRM, catalysts are normally engineered for high surface areas and active metal site dispersions.[18, 19] However, as previously mentioned, the harsh conditions of DRM will result in the instability of the carefully designed catalyst structures, often by aggregation of metal centers, leading to increased rates of coking. Thus, future catalysts must be those which maintain high dispersion during the harsh reaction conditions while achieving the high H_2/CO ratios needed for further use of the syngas produced.

1.2. The role of the support in Ni-based DRM

Ni-based DRM catalysts are supported on a wide range of supports ranging from non-reducible alumina (Al_2O_3) based supports to semi-reducible Ceria (CeO_2) based supports, and the behavior of these catalysts strongly depends on the supports.[5, 16, 20, 21] For example, the site where CO_2 is adsorbed, the reduction temperature of the Ni^{2+}, and the H_2 selectivity are all greatly affected by the support environment, which dictates Ni-support interactions. Thus, it is imperative to elucidate and understand the effects of support on the structure of the Ni particles and the DRM reaction itself.

Ceria has seen considerable attention as a reducible support in the last five decades due to the facile interchange between Ce^{3+}/Ce^{4+} oxidation states, as seen in Figure 1.2.[22-24] This semi-reducible aspect of ceria means oxygen vacancies (OVs) are formed. The vacancies are sites for the adsorption of CO_2, which is reduced to CO, eliminating two vacancies.[25-27] Oxide-CeO_2 mixtures have been widely studied to achieve optimal oxygen storage capacity (OSC) resulting from such redox behavior. By doping the CeO_2 lattice with Zr, an increase in the OSC has been found because the Ce-O bond is weakened when the fluorite crystal structure is distorted by intercalation of the smaller Zr^{4+} ion.[28-30] It is known that for Ce-Zr mixed oxides, 3/1 to 1/1 (molar) Ce/Zr ratios give the largest OSCs and therefore the most potential vacancy formation.[31-33]

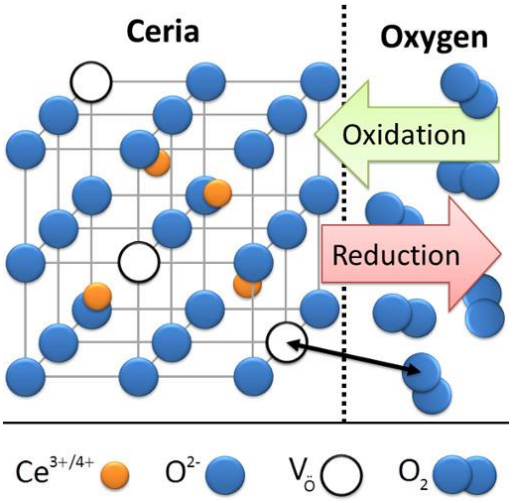

Figure 1.2. Ce^{3+}/Ce^{4+} interchange forming oxygen vacancies.[34]

When zirconia is present in high concentrations, the ceria support loses its fluorite structure in favor of a tetragonal phase; this transition reduces the OSC of the support.[35]

Due to the high oxygen mobility in CZO mixtures caused by incorporating Zr^{4+}, lattice oxygen can readily oxidize surface-deposited carbon.[36] However, if the rate at which the carbon is oxidized is too slow, or if the Ni clusters are too large (causing oxygen diffusion through the nickel to take longer), carbon species can intercalate into the cluster and form carbon filaments.[17, 37] Surface OV also play a role in DRM kinetics by activating the CO_2,which lowers the DRM observed activation energy.[38-41] CO_2 can adsorb on and be reduced by the Ce^{3+} defect sites even without a nearby Ni active center or a hydroxyl- terminated surface [39] However, while the OVs present in ceria and CZO improve DRM activity, OVs also enhance the activity of the RWGS reaction, lowering H_2/CO below one, as shown in Figure 1.3.[27, 42]

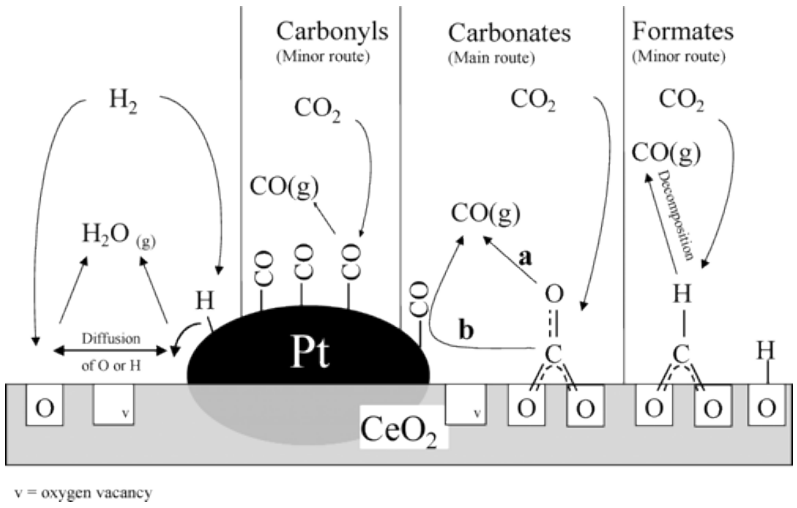

Figure 1.3. Model for the reaction mechanism of the RWGS reaction over Pt/CeO_2[42]

Ni supported on γ-Al_2O_3 has been one of the most studied DRM catalysts due to its ability to achieve high H_2/CO ratios (~1) and provide support mechanical strength and integrity (Yung et al 2009). The non-reducible nature of γ-Al_2O_3 means that CO_2 activation is by reaction with nearby *OH, with or without metals as shown by DFT[43, 44], CO_2 IR[45], and CO_2 TPD[46].High H_2/CO ratios (>0.8) are reported at >700 °C with the use of Ni/γ-Al_2O_3.[47, 48] However, undoped Ni/γ-Al_2O_3 typically cokes rapidly under standard DRM conditions (1:1 CH_4:CO_2, reactant partial pressures ≥ 1 bar), especially at temperatures below 700°C.[49, 50] A significant amount of attention has been given to the modification of the Ni/γ-Al_2O_3 catalyst by adding promoters to reduce the acidity of the support and affect the kinetics of C^* formation on the surface. Magnesium doped into alumina has been shown to reduce the amount of coke formation by reducing the acidity of the Al_2O_3[45], creating more Lewis base sites, which enhance the chemisorption of CO_2.[51, 52] This causes a twofold effect where the CO_2 can react with surface carbon forming CO, and also adsorb on more surface sites. Both effects would enhance DRM activity.[51] TPR analysis of Mg-Al mixed oxides has shown that the addition of Mg to alumina

slightly reduces the reduction temperature of NiO slightly (~ 60°C decrease) through the competition of Mg and Ni for substitution into the alumina lattice. By forming $MgAl_2O_4$ instead of $NiAl_2O_4$, the NiO reduction temperature is reduced.[51]A strong Ni-support interaction is still maintained, as indicated by the high reduction temperatures needed to activate the Ni (>650°C). Due to both of the above characteristics, Mg-Al mixed oxides also have been shown to considerably improve lifetimes (up to 100 h) of DRM catalysts, while showing upwards of a 30% increase in activity.[20, 45, 51, 53]

Combining non-reducible/reducible supports has also seen significant attention for DRM due initially to the success of three-way automotive catalysts that combine CZ oxide mixtures with an Al_2O_3 phase. DRM catalysts combining non-reducible and reducible supports were synthesized by doping Ce into mesoporous Al_2O_3, by creating layered $MgO\text{-}Al_2O_2\text{-}ZrO_2$ oxide mixtures, or by coating Ni/SiO_2 with a ceria overlayer.[54-56] In all three cases, the Ni-support interaction is altered. For instance, Wang et al. found that doping mesoporous Al_2O_3 with Ce improved the DRM activity, with a near 50% increase in TOF seen along with the presence of more OVs near Ce atoms. Similarly, $MgO\text{-}Al_2O_3$ derived from the layered double hydroxide hydrotalcite ($Mg_6Al_2(OH)_{16}CO_3 \cdot 4H_2O$) deposited on ZrO_2 resulted in a 50% increase in CO_2/CH_4 conversions over undoped Ni (2.5wt%)/ZrO_2.[55] Enveloping a Ni/SiO_2 catalyst with a ceria overlayer drastically increased the activity (50% rate increase) and lifetime of the catalyst and reduced its rate of coke formation.[56] Like Ce-doped Al, the $Ni/SiO_2@CeO_2$ catalyst took advantage of ceria OVs. But the overlayer also played a role in maintaining the dispersion of the Ni sites.[56]

1.3. Hydrogen spillover and oxygen reverse spillover on DRM catalysts

It is understood that the selectivity of the DRM process is partly controlled by the RWGS reaction and the rate at which hydrogen is converted to water. On a catalyst such as Ni on a non-reducible support, with little spillover, the combined DRM/RWGS microkinetics can be illustrated as in Figure 1.4. In other words, the overall DRM rate is controlled by methane decomposition as long as [O*] is large enough and the [C*] concentration is not diminished by rapid coking to a non- or less-oxidizable carbon form.[57] But a large [O*] could lead to more [OH*], and therefore it is evident that there is no way to maximize the H_2/CO ratio unless K_5 is low. It would also be desirable to supply [O*] from elsewhere as necessary to minimize any coking.[57] This is the kinetics idea behind an adjacent reducible support, and the reason why it is now often thought that the active transition metal (TM) sites for DRM could be oxygen-rich, i.e., electropositive and at an oxide interface.[25, 27, 56, 58-60] This does not mean the sites are perfectly crystalline NiO, which appears to be mostly inactive for DRM.[60] There are also studies which have come to a totally different conclusion, i.e., the Ni remains Ni(0) even at DRM conditions.[61]

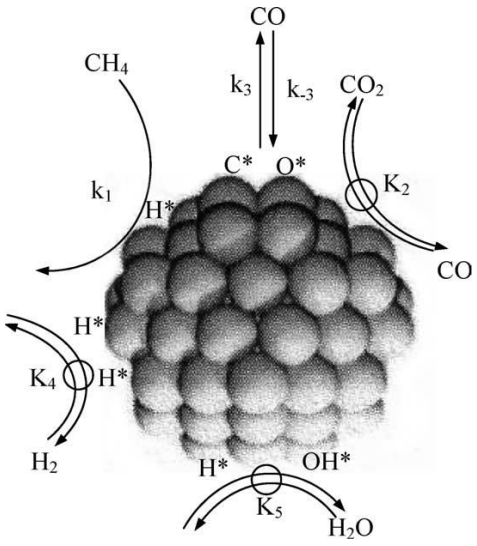

Figure 1.4. Schematic illustrating microkinetics of combined DRM/RWGS on a TM crystallite such as Ni. Single arrow: irreversible step; double arrow, reversible step; circled double arrow, quasi-equilibrated step.[57]

The rates of the DRM and RWGS reactions for Ni on reducible surfaces such as CeO_2 therefore depend upon H-spillover from Ni sites and reverse oxygen spillover from the support.[17, 25, 56, 59] While in theory spillover hydrogen could also react with bulk oxygen or adsorbed CO_2, the likelihood of either is small, because supports such as CeO_2 or MgO cannot form either hydrides or carbonates at temperatures typical of DRM. But the spillover H-atoms could easily react with hydroxyl-rich surfaces to make water (large K_5, just on a different surface), accelerating RWGS. This is why the H_2/CO ratios on reducible supports can be low, even though they can be terrific at limiting coking.

Hydrogen spillover onto reducible surfaces has been shown using Pd/CeO_2 and Pt/CeO_2. In the Pd supported case, the magnetic susceptibility as the sample was contacted with H_2 at 294 K gradually increased . Initially this was ascribed to the reduction of Pd^{2+} to Pd^0, but such reduction did not increase the magnetic susceptibility. However, the susceptibility increased three-fold upon reduction of Ce^{4+} to Ce^{3+}.[62] Once the paramagnetic Pd^0 was accounted for, the

amount of ceria reduced was calculated to be 23%. Pure ceria reduces at ~473 K, therefore, it appears that Pd decreases the ceria reduction temperature significantly.[62] This phenomenon was also observed on Rh/CeO_2.[62] Resonant photoemission spectroscopy (RPES) was used to observe hydrogen spillover on Pt/CeO_2. RPES measures the valence band photoemission spectra at photon energies corresponding to the 4d to 4f resonance in the Ce^{3+} or Ce^{4+}. The resonant enhancements for Ce^{3+} and Ce^{4+} were quantified. The ratio of Ce^{3+} to Ce^{4+} is labeled the resonant enhancement ratio (RER). The RER was measured as Pt/CeO_2 was annealed stepwise from 150 to 300 K, after being exposed to 50 Langmuirs of hydrogen at 150 K. A maximum of the RER was observed at 250 K.[63]

While the effects of H_2 spillover have typically been studied on reducible surfaces, recent studies have also demonstrated hydrogen spillover on a non-reducible Al_2O_3 surface.[64] X-ray absorption spectroscopy (XAS) was used to quantify spillover by measuring variations in the Fe L_3 edge upon increasing the distance between Pt and Fe_3O_4 islands supported on Al_2O_3. Pt was the H-atom source, while Fe_3O_4 was an easily reducible probe to measure the distance the H_2 atoms would travel to reduce it, as shown in Figure 1.5. As the distance from the Pt island increases, the shoulder at 708 eV in the XAS disappears, indicating that as Fe_2O_3 is placed further from the Pt islands, it is reduced less until, at 45 nm, it is no longer reduced. This experiment elucidated the limited mobility of H-atoms on an Al_2O_3 surface. Alternatively, the group ran the same experiment on a TiO_2 surface, and complete Fe_2O_3 reduction was seen at all distances. Using these experiments, the hydrogen mobility was calculated via DFT on Al_2O_3; H-atoms diffused across the surface at ~10^{-23} cm^2s^{-1} at 300 K, which was ~10^{10} cm^2s^{-1} slower than hydrogen diffusion on TiO_2. The rate of carbon atom diffusion across an Al_2O_3 surface was found to be ~10^{-14} cm^2s^{-1}.[65] This drastic difference in diffusion rates suggests that a barrier of

Al_2O_3 could significantly inhibit hydrogen spillover from Ni. There are few reports of a non-reducible overlayer atop a Ni/CeO_2 or similar highly reducible supported catalyst.

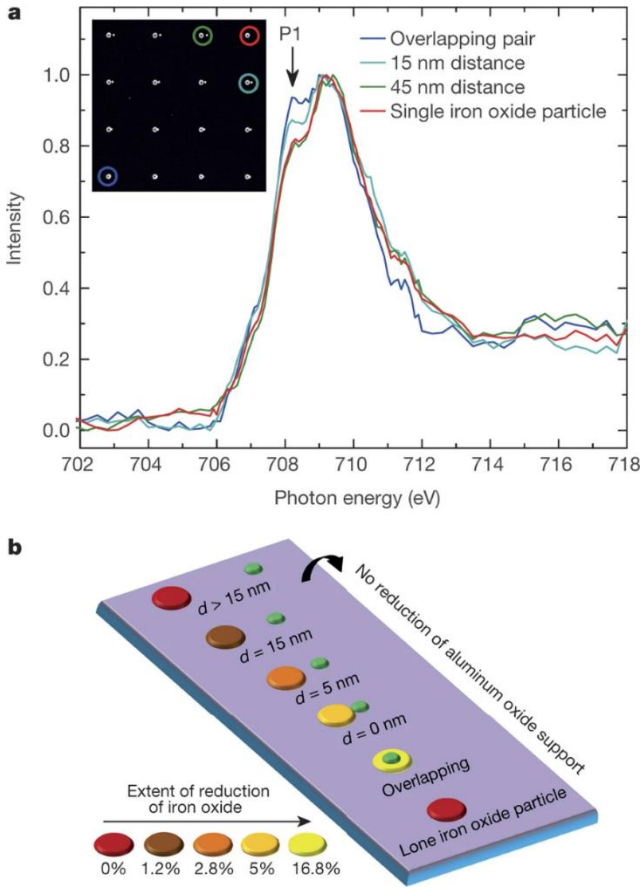

Figure 1.5. a) Fe L_3 XAS spectra of Fe_3O_4-Pt cluster with increasing spacing. The shoulder at 708 eV disappears once the spacing exceeds 15 nm, indicating limited surface diffusion of H-atoms after spillover. b) Cartoon showing the extent of reduction for different particle spacings.[64]

1.4. Atomic layer deposition to create thin shells

Using a shell layer to confine Ni during DRM has seen much attention due to its ability to inhibit the strong sintering effect at elevated temperatures (especially at >700°C). Atomic layer deposition (ALD) is a highly controllable self-limiting surface reaction method for the deposition of oxide layers. ALD offers conformality due to the self-limiting nature of the technique.[66] The technique employs an A-B binary reaction method, which consists of completely saturating the reaction chamber with a MO precursor and then purging and subsequently converting the precursor to a hydroxide by saturating the reaction chamber with steam. The ALD process can lead to high conformality and control of the thickness at an atomic scale.[67-70]

The A-B binary reaction to deposit Al_2O_3 is that of trimethylaluminum (TMA) and water.[71] The first step involves pulsing TMA into the ALD reaction chamber, where it reacts with the hydroxyl (-OH) terminated surface, producing a methane byproduct in the process, as seen in equation 1.5. This reaction occurs until all the surface -OH groups are consumed. Second, the chamber is purged to eliminate the excess TMA and byproduct methane. The third step involves pulsing water vapor into the reaction chamber, which reacts with the methyl groups on the AlO_x surface, as shown in equation 1.6. This step forms a newly -OH terminated surface that can restart the ALD process if another layer is required. Lastly, the byproducts of methane and water are purged from the chamber. A cycle involves all four steps, and typically one cycle of Al_2O_3 ALD results in 1.2Å of growth at 200°C.[71] It is crucial that, once the desired layer thickness is achieved, a calcination step follows the ALD to form pores in the oxide overlayer, exposing the TM catalytic sites.

$$-OH^* + Al(CH_3)_3(g) \rightarrow -OAl(CH_3)_2^* + CH_4(g) \qquad \text{eq1.5}$$

$$-OAl(CH_3)_2^* + 2H_2O(g) \rightarrow -OAl(OH)_2^* + 2CH_4(g) \qquad \text{eq1.6}$$

ALD overlayers have been used as barriers to counteract deactivation during catalytic reactions. Lu et al. developed hierarchical Pt/Al_2O_3 catalysts that prevented deactivation during propane dehydrogenation by depositing a thin Al_2O_3 layer over the Pt by ALD.[72] The catalysts were annealed in air up to ~1200°C to generate pores in the surface layer and expose the Pt clusters. Although the group did observe a loss in surface area and pore volume due to the high annealing temperatures, the ALD layer deposited on uncoordinated Pt sites acted as a Pt particle aggregation barrier, while maintaining high selectivity to propylene.

The efficacy of thin shell layers such as those produced by ALD or other core-shell techniques for DRM is open to dispute. While some core-shell catalysts (Ni initially deposited on the core) have shown impressive turnover frequencies, such as the previously mentioned $Ni/CeO_2@SiO_2$ catalyst (TOF~1.9 s^{-1})[56], it is not known if these are truly layered materials, or if oxide (or Ni) mixing into the shell is taking place. A properly synthesized ALD catalyst would show complete oxide segregation, at least initially.

Research on ALD for Ni-based DRM catalysts remains scarce with most of the work done on coating Ni/Al_2O_3 catalysts with an oxide overlayer to prevent the aggregation of Ni particles.[21, 73, 74] There is debate about using alumina ALD overlayers for Ni-based catalysts due to the possible formation of $NiAl_2O_4$, which is known to be inactive for DRM.[21, 75] Alucone, a hybrid aluminum-based organic-inorganic film made using TMA and ethylene glycol as precursors, was used in ALD to overcoat Ni.[73] The Alucone overlayer was calcined at 500°C for 1 h to create a porous structure. The sample was reduced at 500°C for 1 h following the

oxidation. The DRM reaction was run at 700°C. Using ten ALD cycles, a decrease in Ni nanoparticle ripening was observed, 5.3 to 7.8 nm over 108 h for the ALD-coated catalyst, compared to 5.3 nm to 9.7 nm over 82 h for the uncoated catalyst.[73] The effects of conventional alumina and alucone overcoats on Ni catalysts for DRM were compared.[76] The increase in activity and stability using the ALD overcoat was minimal at best and attributed to the formation of $NiAl_2O_4$. In contrast, alumina ALD over Ni/Al_2O_3 catalysts was found to decrease the rate at which sintering and coke formation occurred, as shown in Figure 1.6a.[21] Additionally, it was found that any initial $NiAl_2O_4$ would reduce under DRM conditions to Ni/Al_2O_3, slowly increasing the catalytic activity, as shown in Figure 1.6b. Similar work using five cycles of alumina ALD over a 20 wt% Ni/Al_2O_3 catalyst showed a drastic decrease in Ni particle aggregation;[77] the average particle size for the uncoated catalyst increased from 8.5 to 24.5 nm during 40 h of DRM, while the ALD-coated sample maintained its original average particle size of 8.7 nm. However, the catalysts still deactivated rapidly after reaching maximum activity, bringing into question the efficacy of these alumina over alumina ALD complexes.

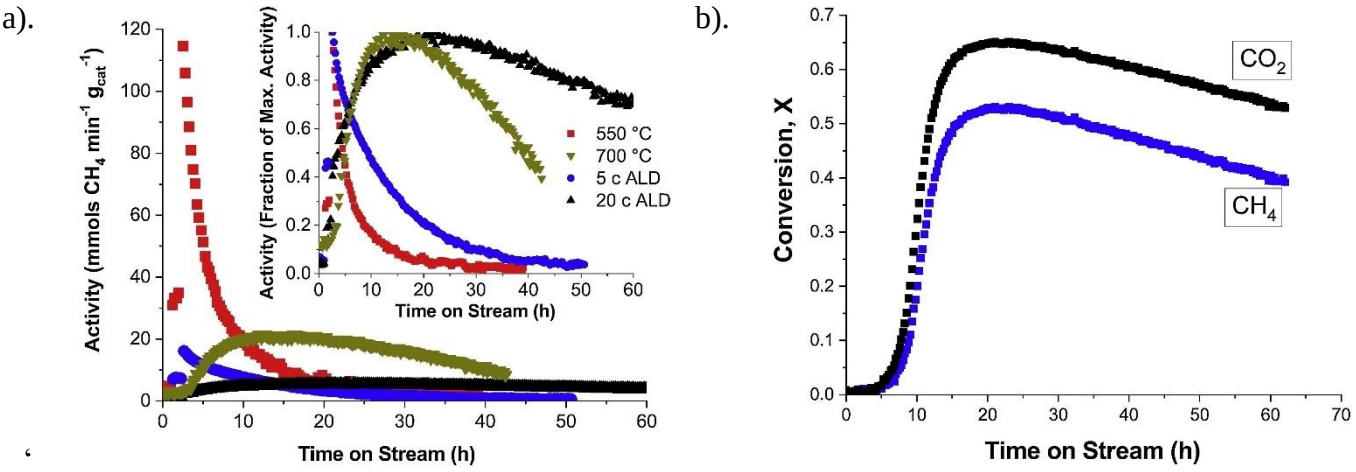

Figure 1.6. a) Activity of Ni/Al_2O_3 catalysts calcined at 550°C with and without an alumina ALD overcoat and calcined at 700°C with an overcoat. Inset shows the same data normalized to the fraction of the maximum activity for each sample. T=700°C b) DRM activity of $NiAl_2O_4$. T=700°C[21]

Extending the above ALD work to CZO-based DRM systems has yet to be done. Exploration of the effects of ALD overcoats on the activity/selectivity/stability of Ni/CZO catalysts, both non-reducible (Al_2O_3) and semi-reducible (TiO_2), is the subject of this thesis.

1.5 Scope and Proposed Work

In this work, ALD coated Ni:CZA (ceria-zirconia-alumina mixed oxide) is prepared using Al_2O_3 ALD deposition to create highly stable catalysts with a non-reducible/reducible hierarchical core-shell structure. The synthesis produces an initially highly controlled shell layer, which can be modified by changing the ALD precursor and number of cycles. DRM catalytic activity, selectivity, and stability of different ALD-coated samples were compared to uncoated counterparts. Before any long-term catalytic testing, samples were screened by rapid thermogravimetric analysis (DSC/TGA). Overlayer thickness was varied to determine the optimum layer thickness for high stability, selectivity, and activity. Long-term high conversion packed bed reactor experiments were used to further assess the effects of the ALD overlayer. Pre-DRM characterizations consisting of X-ray diffraction (XRD), porosimetry, and X-ray absorption spectroscopy (XANES and XAFS) were performed to understand the structural and electronic states in the initial catalysts. Post-run characterization used the same methods to study changes in catalyst structure upon reaction. It is found that adding a five-cycle ALD layer improves catalyst lifetime by reducing the coking rate and keeping the Ni clusters small.

To further understand the effects of the ALD layers, transmission electron microscopy (TEM) and pulsed CO_2/CO diffuse reflectance infrared Fourier transform spectroscopy (DRIFTS-FTIR) were performed at Oak Ridge National Laboratory in order to determine the oxidation states of O-atoms, the overlayer morphology, the aggregation state of Ni, and to

understand how the overlayer affects the absorption of CO_2/CO on the CZA support. Understanding how the overlayer affects the catalyst before, during, and after reaction enables optimization of overlayer deposition to create more active, selective, and stable DRM catalysts.

Chapter 2. Experimental Section

2.1. Materials

Commercial CZA40 (Al_2O_3 40.07 wt%, ZrO_2 23.59 wt%, CeO_2 33.47 wt%, La_2O_3 1.45 wt%, Y_2O_3 1.42 wt%, Lot #CZLYA40-150802-AJ) catalyst support was supplied by PIDC, nickel nitrate hexahydrate ($Ni(NO_3)_2*6H_2O$, Sigma Aldrich, 99%), trimethylaluminum ($Al(CH_4)_3$, Sigma Aldrich, 97%), titanium(IV) isopropoxide ($Ti[OCH(CH_3)_2]_4$, Sigma Aldrich 99%), and urea (CH_4N_2O, VWR, ACS grade) were used as received. The reactant gases were CH_4 (Airgas, 99%), and CO_2 (Airgas, 99%). Air (Airgas, breathing grade), N_2 (Airgas, UHP) and 5% H_2 (Airgas, certified) were also used for calcinations/reductions.

2.2 Adsorptive Deposition

An adsorptive deposition (sometimes called "strong electrostatic adsorption") was used to deposit Ni onto the CZA40 support, as adapted from previous work[16, 78]. Powdered CZA40 was added along with the desired amount of $Ni(NO_3)_2•6H_2O$ and 30ml of 0.3M urea per gram support. The solution was stirred and reacted for 24 h under reflux at 90 °C. The product powder was washed with DI water and dried at 100 °C overnight. The dried powder was reduced for 6 h in 5%H_2/95% N_2, with a ramp rate of 10°C/min.

2.3. Atomic Layer Deposition

An alumina ALD method was adapted from previous work.[79] AlO_x overcoats were deposited using a bench-top viscous-flow ALD reactor (GEMstar XT) at 150 °C by alternating exposure of trimethylaluminum (TMA) and water vapor using N_2 as both carrier and purge gas, where both TMA and water bubblers were kept at room temperature. Each AlO_x cycle consisted of 90 s of TMA exposure followed by 90 s of water exposure, followed by 300 s of N_2 purge

(90-300-90-300). Three and twelve cycles of AlO_x ALD were performed on Ni/CZA40. The mass gain was obtained by weighing the powder before and after ALD. Samples are referred to by the mass gain from ALD, as 0.3, 0.5 or 1.2 nm AlO_x ALD.

2.4. X-ray Diffraction (XRD)

Powder X-ray Diffraction (XRD) was performed to analyze the structure and bulk crystalline phases of the as-synthesized and used catalyst samples. Diffractograms were collected using a PANalytical XRD at 45 kV and 40 mA. Spectra were recorded at 0.04° steps over the range 5-70°, with a dwell time of 60 s. A Cu K_α radiation source was used. The average crystal size of an identified phase was calculated using the Scherrer equation ($D = \frac{K\lambda}{\beta \cos(\theta)}$), where K is the dimensionless shape factor, typically set at .9, λ is the x-ray wavelength for Cu K_α radiation, and β is the full-width at half maximum of the XRD peak used for the analysis.

2.5 N_2 Porosimetry

The surface area, total pore volume, and pore size distributions of the fresh and used catalysts were measured by N_2 adsorption using a Micromeritics ASAP 2020 Plus porosimeter. Samples were dried at 300 °C and degassed prior to analysis. The surface area was determined by the BET method, and the pore size distribution was determined using the BJH method.

2.6. High-Resolution Transmission Electron Microscopy (HRTEM) and Energy Dispersive X-ray (EDX) Spectroscopy

Morphology and size of the catalysts were analyzed by HRTEM using a 200 kV JEOL NEARM electron microscope equipped with double aberration correctors, a dual-energy-loss spectrometer, and a cold FEG source. Before imagining, the samples were dispersed in ethanol and drop cast on a 300 mesh, lacey carbon grid. EDX was performed using an FEI Quanta 3D

FIB microscope equipped with an EDAX Apollo XL EDX detector operating at an accelerating voltage of 20 kV and a current of 4 nA. Image J (version 1.53k) was used to analyze lattice spacings of imaged catalysts.

2.7. X-ray Spectroscopies

X-ray photoelectron spectroscopy (XPS) was performed to determine the amounts of oxygen vacancies and the Ce^{3+}/Ce^{4+} concentration ratios. XPS was performed using a Scienta Omicron ESCA 2SR equipped with a monochromatic Al K_α ($h\nu$=1486.6 eV) X-ray source and a hemispherical analyzer with a 128-channel detector at 1.3 x 10^{-9} torr. The Gaussian width of the photon source was 0.5eV with a focus voltage of 300 V. The adventitious carbon C 1s peak at 284.4 was used to calibrate the energies. After Shirley background subtraction, all peaks were fitted using Casa XPS (version 2.3.25) as Gaussians.

X-ray Absorption spectra (XAS) was performed to analyze the local coordination of the Ni metal centers. XAS was performed at the LSU Center for Advanced Microstructures and Devices (CAMD). Some Ni K-edge spectra were taken at the HEXAS beamline, using a Ge 220 double crystal monochromator, collected at room temperature in fluorescence mode with a Ni foil calibration standard. Other Ni K-edge spectra were taken at the WDCM 2.0 beamline equipped with a Si 111 channel-cut monochromator in fluorescence mode, and also calibrated with a Ni foil standard. Integration time was adjusted to obtain adequate counts up to wavenumber 12. Runs were repeated to improve counting statistics. Both X-ray absorption near-edge (XANES) and X-ray absorption fine structure (XAFS) spectra were collected.

Background subtraction, deglitching, and merging of spectra of XANES data were done using Athena 0.9.061. Ni K-edge XAFS fitting was performed in Artemis 0.9.26. Four parameters were varied to obtain the best possible fits of the Ni K-edge data, S_0^2 (amplitude

reduction factor), σ^2 (Deby-Waller factor), ΔE_0 (deviation in E_0 caused by structural deviations from the ideal crystal structure), and ΔR (deviation in the interatomic distance). A NiO standard was fit first to get information on S_0^2 with known coordination numbers and ΔR's. The fitting range in R space was 1-5Å, and all significant scattering paths were included.

2.8. Catalytic Activity Screening

The catalytic activity of the various ALD-coated and uncoated catalyst samples were measured using a TA SDT Q600 Differential Scanning calorimetry (DSC)/Thermogravimetric Analyzer (TGA). ALD-coated catalysts were first pretreated in air (100 mL/min) at 600°C for 1 h to remove residual water and generate pore space in the overlayer. Then the samples were reduced in 5% H_2/95% N_2 for 3 h. The DRM reaction (135 mL/min total flow, 0.25 atm partial pressure CH_4 and CO_2, 0.5 atm N_2) was performed at 650 and 750 °C for 1.5 hours at each temperature. The heat flux and change in mass were both measured. The heat flux is roughly the heat evolved by the DRM reaction, and the weight change can be related to the coking rate.[16] Heat flow data were used in an Aspen HYSYS program to calculate the reforming rate and methane conversion from this experiment.

2.9. DRM in Fixed-Bed Reactors

Catalysts that showed promising activity results in the TGA screening method were tested in a fixed-bed reactor. The fixed bed reactor is a 1/2" quartz reactor tube with α-alumina and quartz wool as the packing material. Catalyst weight was varied between 0.35-0.25 g to vary the GHSV. The reactant flow is 1:1 CH_4:CO_2 (molar) at higher partial pressures than the TGA experiment (~0.65 atm each). The reactor setup in this work is the same as in previous work. [1] An Agilent 6890N GC-MS was used to analyze the outlet gas composition. The reactor tube is

heated by a furnace (Teco F-5-1000, 320 watts) whose temperature is controlled by a Eurotherm 818P PID controller. Figure 2.1 shows a schematic of the reactor setup.

Conversion, yield, and selectivity from these experiments were calculated using an extent of reaction method. Three equations represent the main reactions (DRM, water-gas shift, and coking) as follows:

$$CO_2 + CH_4 \leftrightarrow 2H_2 + 2CO \quad \xi_1$$

$$CO_2 + H_2 \leftrightarrow H_2O + CO \quad \xi_2$$

$$C + H_2O \leftrightarrow H_2 + CO \quad \xi_3$$

The ξ's are molar extents of reactions for these three reactions in mol/min, and they were calculated by solving the component mass balances simultaneously, using both the compositions and the effluent flow rate. These results were refined using a nonlinear regression method where the objective function is the sum of the squared residuals of the CH_4, CO_2, H_2O, CO and H_2 mass balances. The terms $F_{in,CH4}$, and $F_{in,\,CO2}$ are molar flowrates of the feed components in mol/min. The yields of products on an elemental carbon basis and the conversions of CH_4 and CO_2 are calculated as follows:

$$Y(CO) = \frac{2\xi_1 + \xi_2 + \xi_3}{F_{in,CH4} + F_{in,CO2}}$$

$$Y(C) = \frac{-\xi_3}{F_{in,CH4} + F_{in,CO2}}$$

$$X(CH_4) = \frac{\xi_1}{F_{in,CH4}}$$

$$X(CO_2) = \frac{\xi_1 + \xi_2}{F_{in,CO2}}$$

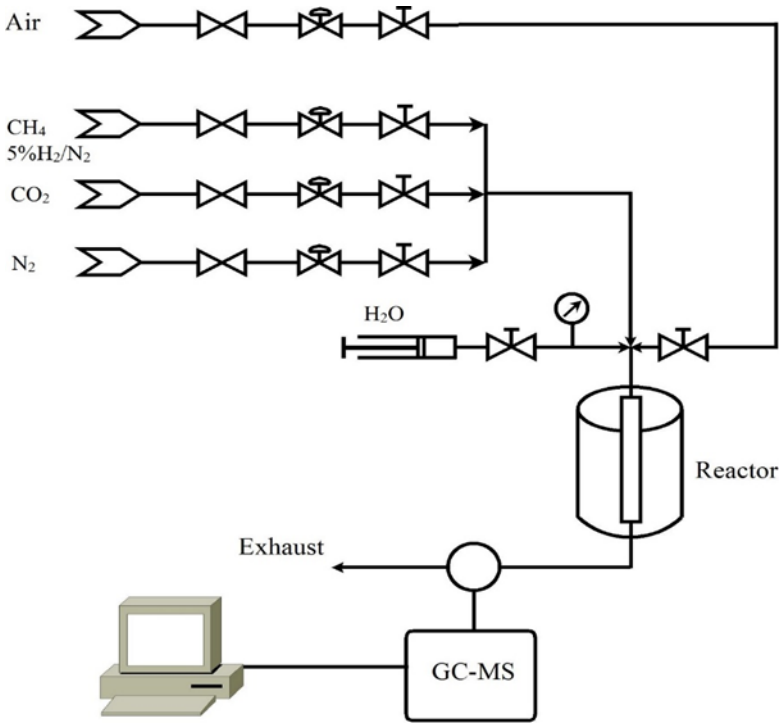

Figure 2.1. Schematic of the reactor system for DRM. GC parameters in appendix A[16]

Chapter 3. Improved Selectivity and Stability in Methane Dry Reforming by Atomic Layer Deposition onto Ni-CeO_2-ZrO_2/Al_2O_3 Catalysts

Uncoated Ni-CZA40 (5 wt% Ni) was the reference material for this study. Initial characterization of fresh Ni-CZA40 was by XRD and N_2 physisorption. The diffraction peaks (Figure 3.1) of the Ni-CZA40 powders were indexed to cubic CZO (ICSD 157416)[80], with no observable peaks corresponding to Ni or NiO, indicating the highly dispersed nature of Ni in the fresh catalyst. The CeO_2 crystallite size was calculated (using the Scherrer equation) to be 5.5 nm for the Ni-CZA40 powder sample based on the (111) reflection. The N_2 physisorption gave a surface area of 95 m^2/g by the BET method with a total pore volume of 0.64 cm^3/g.

Ni-CZA40 was tested catalytically in the fixed bed reactor system at 750°C with a reactant flow of 1:1 CH_4:CO_2 (at partial pressures of ~0.65 atm for each reactant) and a gas hourly space velocity (GHSV) of 37000 mL/(h•gcat). The catalyst exhibited initial conversions of 55% for CO_2 and 44% for CH_4 with an H_2/CO ratio of 0.75, as shown in Figure 3.2. At 16 h time onstream at these conditions, an increase in reactor pressure was seen, indicating the presence of large quantities of carbon (coke) beginning to block the reactor. The final conversions were 52% for CO_2 and 39% for CH_4, with an H_2/CO ratio of 0.69. These low H_2/CO ratios indicate a significant rate of RWGS at these conditions.

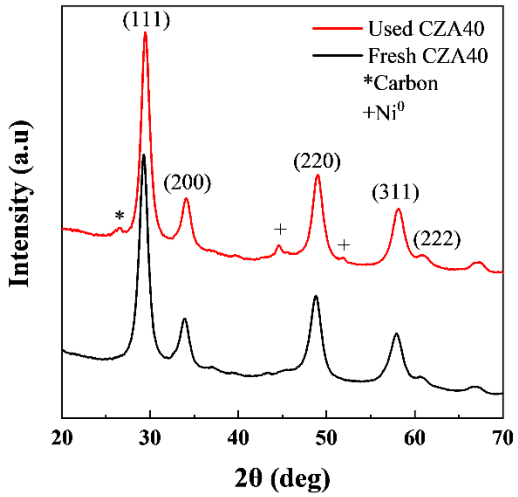

Figure 3.1. XRD spectrum of Used (red) and Fresh (black) Ni-CZA40. Stars indicate peaks indexed to carbon. Plus signs indicate Ni^0 peaks.

XRD analysis of the used Ni-CZA40 (Figure 3.1) revealed the emergence of two additional crystalline phases. The peak at 26.5° is indicative of semi-graphitic carbon formation on the catalyst[16], while the peaks at 44.7° and 51.8° are indicative of the formation of Ni^0 clusters[16]. The CeO_2 crystallite size was calculated (using the Scherrer equation) to be 6.6 nm for the used Ni-CZA40 powder sample based on the (111) reflection; the increase in Ce (111) crystal size is due to support sintering. The presence of both Ni^0 and carbon crystalline phases confirms that the catalyst was being structurally altered by both coking and sintering of the Ni metal sites, and while these changes were insufficient to deactivate the catalyst significantly (Fig. 3.2), they were sufficient to reduce its selectivity and to lead to a situation where the process would have become untenable due to gross coke formation. A temperature programmed oxidation was done on Ni-CZA40 used catalyst to examine the amount of coke deposited during DRM, and a coking rate of 2.1 x 10^{-4} mmol C/(mg_{cat}• h) was found.

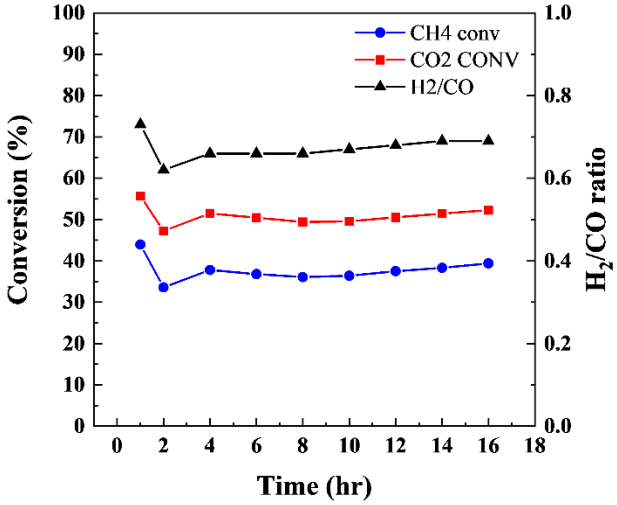

Figure 3.2. DRM test of Ni-CZA40 (5wt% Ni), 1:1 CH_4:CO_2 feed mixture at 750°C, 1.2 bar, 37000 GHSV.

Therefore, different ALD overlayers were deposited over the Ni-CZA40 catalyst in order to test their effectiveness in suppressing clustering of the Ni during DRM and also in suppressing the RWGS reaction, to better achieve the theoretical maximum H_2/CO ~1 for DRM with no RWGS or coking reactions. Both Al_2O_3 (5, 9 and 20 wt% deposited as amorphous boehmite, then converted to Al_2O_3) and TiO_2 (15 wt% deposited as amorphous $Ti(OH)_2$) overlayers were prepared, at nominal film thicknesses (0.3, 0.5 and 1.2 nm for Al_2O_3) that assume both conformality of the overlayer and the generation of a γ-Al_2O_3 bulk structure. One cycle of ALD deposits 1.5-2 Å for nanoparticle systems.[79, 81] The 9 wt% deposition took 3 cycles, giving an assumed nominal film thickness of 0.5nm. The other film thicknesses were calculated by taking the ratio of actual wt%/9 wt%. For example, 5 wt%/9 wt% is 60% so the 5 wt% catalyst has 60% of the layer thickness of the 9 wt%.

A rapid TGA/DSC screening method at low CH_4/CO_2 conversions was used to determine short-term effects on the activity/stability of the Ni-CZA40; this method was adopted unchanged

from previous work[5, 16]. These samples along with Ni-CZA40 itself were screened in the TGA/DSC with results as shown in Table 3.1. The ALD samples were first pretreated by calcining the samples at 600°C under air for 1 h, then a reduction at 600°C using 5% H_2/N_2 for 3 h, while the Ni-CZA40 sample was just reduced at 600°C using 5% H_2/N_2 for 3 h. As the heating flux of a DSC is directly proportional to the DRM reaction rate in the absence of significant RWGS reaction, the reforming rate can then be calculated from the heat flux using the Aspen HYSYS® process simulator[82]. The neglect of any effects of the RWGS on the heat flux is justified both by its relative thermoneutrality compared to DRM, and the knowledge that the RWGS rates are always less than DRM rates (an assertion to be tested later)[16]. For example, the calculated (by HYSYS) endothermic heat of reaction for DRM is 7.2-7.5 times that of RWGS over the temperature range 650-800°C. The coking rate was determined by the weight change over 1.5 h observed after the first 0.5 h of reaction.

Table 3.1. Catalyst performance metrics of Ni-doped CZO and Ni-CZO coated with Al_2O_3. DRM rate in mmol/(mg cat•h). Coking rate in mg coke/(mg cat•h).[1]

Catalyst	DRM rate, 750°C	DRM rate, 650°C	Coke rate, 750°C	Coke rate, 650°C
Ni-CZA40	0.21	0.14	1.3×10^{-2}	4.5×10^{-3}
0.3nm ALD-Ni-CZA40-PR[2]	0.21	0.05	-3.5×10^{-3}	2.3×10^{-2}
0.5nm ALD-Ni-CZA40	0.23	0.12	1.5×10^{-2}	-3.5×10^{-3}
0.5nm ALD-Ni-CZA40-PR[2]	0.36	0.15	-2.0×10^{-3}	-2.0×10^{-3}
1.2nm ALD-Ni-CZA40-PR[2]	0.15	0.05	-1.8×10^{-3}	-3.2×10^{-3}
0.5nm TiO_2-Ni-CZA40	0.15	0.077	-2.0×10^{-3}	-2.3×10^{-3}

[1] The coking rate was measured at > 0.5 h into the run, but in some cases the weight was still decreasing. This denotes an essentially zero rate of coking.
[2] PR stands for pre-reduced at 550°C with 5% H_2/N_2 for 3 h.

The addition of the Al_2O_3 overlayer at nominal 0.5 nm thickness did increase the reforming rate at 750°C, while little to no benefit was seen at 650°C. A negative coking rate, like the ones observed at 650°C for the Al_2O_3 overlayers, indicates slow structural changes are taking place which reduce the total adsorbate load on the surface. The application of a TiO_2 layer significantly decreased the activity of the Ni-CZA40 at both temperatures and was not investigated further. Reducing the Ni-CZA40 at 550°C with 5% H_2/N_2 for 3 h before layer deposition was also investigated. The sample is labeled as 0.5nm Al_2O_3 ALD-Ni-CZA40 PR. The same TGA pretreatment for ALD samples of oxidation and reduction as listed above was used for the pre-reduced sample. The pre-reduction was found to greatly increase the reforming rate at 750°C to 0.36 mmol $CH_4/(mg_{cat}\bullet h)$. The coking rate of the pre-reduced ALD sample was found to be negligible at 750°C compared to the non-pre-reduced ALD sample. All further ALD coated samples were pre-reduced before deposition.

At 650°C, the DRM rates of the 0.3 and 1.2 nm ALD Al_2O_3 samples were lower by a factor of three compared to uncoated Ni-CZA40. The DRM activity at 750°C was comparable to uncoated Ni-CZA40 for the 0.3 nm sample, while the 1.2 nm coated sample had a lower activity. Both 0.3 and 1.2 nm catalysts showed negligible coking rates at 650 and 750°C. Because the 0.3 and 0.5 nm catalysts appeared to show the most promise for long-term DRM operation, these were further tested at high conversion in the bench-scale reactor system.

The 0.5nm ALD-Ni-CZA40 was first tested at a GHSV of 10900 mL/(h•gcat) at 750°C (Figure 3.3). The sample activated for more than 50 h before reaching its maximum activity and H_2/CO ratio. After this time onstream, it exhibited ~75% CH_4 conversion with an H_2/CO ratio of 0.98. This H_2/CO ratio is greater than the equilibrium H_2/CO ratio of 0.94 calculated using an Aspen HYSYS simulation of the process, including only the DRM and RWGS reactions. The run

was continued to 130 h time onstream, with no deactivation seen in that time. The GHSV was then scaled up to the 37000 mL/(h•gcat) and run for four extra hours (Figure 3.4). While the CH_4 conversion and H_2/CO ratio initially saw a drop in value, the catalyst eventually attained nearly identical conversion and selectivity as at 10900 GHSV. This indicates the catalyst was operating in a diffusion-limited regime at the lower space velocity. Comparing these results to Fig. 3.2, the 0.5 nm ALD overcoat enhanced the DRM activity over the uncoated sample, increasing the CH_4 conversion from 40% (uncoated Ni-CZA40) to 77%, while also increasing the H_2/CO ratio from 0.7 to 0.98. A temperature programmed oxidation was done on the 0.5nm ALD-Ni-CZA40 used catalyst to examine the amount of coke deposited during DRM, and an average coking rate of 3.5 x 10^{-5} mmol C/(mg_{cat}• h) was found, which is an order of magnitude lower than the uncoated Ni-CZA40 sample's coking rate of 2.1 x 10^{-4} mmol C/(mg_{cat}• h).

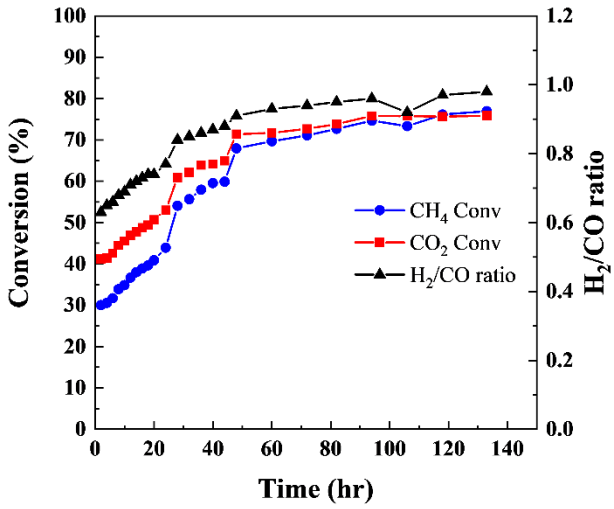

Figure 3.3. DRM test of 0.5nm ALD-Ni-CZA40, 1:1 CH_4:CO_2 feed mixture at 750°C, 1.2 bar, 10900 GHSV.

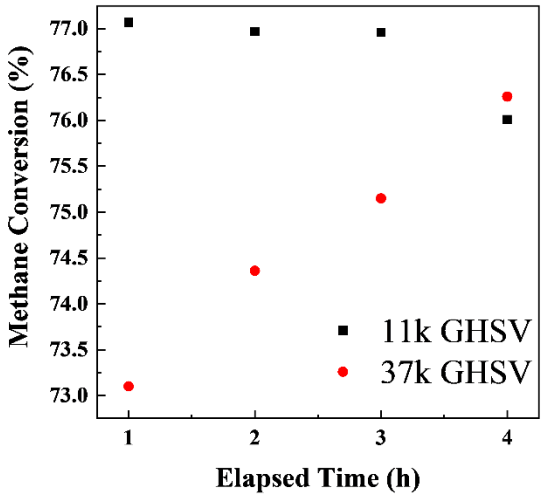

Figure 3.4. DRM test of 0.5nm ALD-Ni-CZA40, 1:1 CH_4:CO_2 feed mixture at 750°C, 1.2 bar. Comparing the four final samples at GHSV 11000 (taken at 137-140 h time onstream) to the first four samples at GHSV 37000, after a change from GHSV 11000 to GHSV 37000.

The 0.3nm ALD-Ni-CZA40 catalyst was also tested in the reactor system at 37000 GHSV (Figure 3.5). The catalyst's induction period was 24 h after which it ran for 109 h with no deactivation. The final averaged CH_4 conversion was 74% with a 0.94 H_2/CO ratio, values only slightly below that of 0.5nm ALD-Ni-CZA40. 4

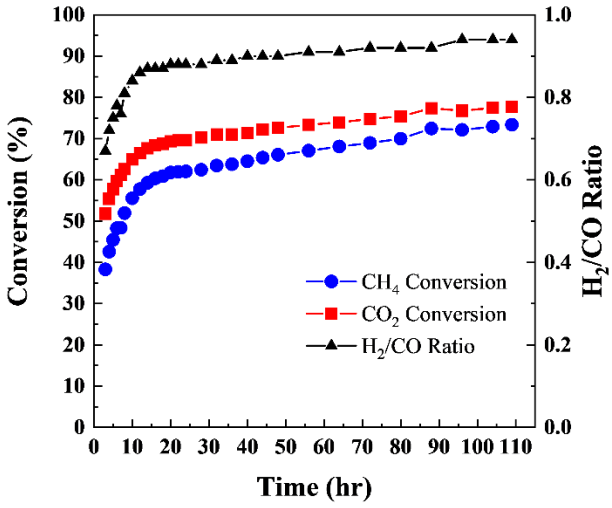

Figure 3.5. 0.3nm ALD-Ni-CZA40, DRM of a 1:1 CH_4:CO_2 mixture at 750°C, 1.2 bar, 37000 GHSV.

Evaluation of the effects of the Al_2O_3 ALD overlayer on the RWGS reaction at partial pressures of 0.26 atm H_2 : 0.26 atm CO_2 : 0.48 atm N_2 was studied using a TGA/DSC method like the DRM screening method shown above in Table 1. The sum of the partial pressures of H_2 and CO_2 in this experiment would be approximately the maximum sum in the larger reactor, so this is a worst-case test for the undesired RWGS reaction. The heat flow values measured using the TGA/DSC are highly characteristic of only the RWGS reaction. To prove this, an Aspen HYSYS simulation was run to compute the equilibrium conversions and heat flows of the RWGS at high CO_2 and H_2 partial pressures along with the main competing reaction, which would be CO_2 hydrogenation (the Sabatier reaction). At 650°C the RWGS contributed 95% of the total heat flow and at 750°C the RWGS contributed 99.5% of the total heat flow. Thus, it is assumed that the CO_2 hydrogenation reaction to CH_4 is negligible for these TGA/DSC experiments. Using the heat flow measurements and Aspen HYSYS, the H_2 conversions for the TGA/DSC experiments were calculated. These H_2 conversions were used to compute rate

constants from the CO_2 mass balance for a 2nd order RWGS reaction assuming plug flow with volumetric expansion (equation 3.1).

$$Da = 2\varepsilon(1+\varepsilon)\ln(1-X) + \varepsilon^2 X + \frac{X(1+\varepsilon)^2}{(1-X)} = \frac{kC_{a0}W}{F'} \qquad \text{Eq 3.1}$$

Where Da is the Damkohler number, a ratio of reaction rate to convective mass transport rate, ε the expansion factor (here, 0), F′ the total volumetric flow rate, and X is the fraction conversion. Using the fractional conversion obtained from Aspen HYSYS, the RWGS rate constant was calculated. The addition of the 0.5 nm ALD overlayer to Ni-CZA40 catalyst results in a 38% decrease in the RWGS rate constant (3.7×10^4 for Ni-CZA40 → 2.3×10^4 0.5nm for ALD-Ni-CZA40) at 750°C and at 650°C a 57% decrease. These rate constants are for equal partial pressures of H_2 and CO_2 (0.26 atm H_2: 0.26 atm CO_2: 0.48 atm N_2) which is only a slightly lower product of reactant pressures than the maximum possible in the bench scale reactor (0.068 atm^2 here vs. 0.09 atm^2 for the bench scale reactor at a feed pressure of 1.2 atm and a fractional conversion of 33%).

Table 3.2. Rate Constants of Ni doped CZA and Ni CZA coated with Al_2O_3.
DRM and RWGS rate constants in $mL^2/(min \bullet mg_{cat} \bullet mmol)$

Catalyst	k_{DRM} , 750°C	k_{DRM}, 650°C	k_{RWGS} , 750°C	k_{RWGS}, 650°C
Ni-CZA40	3.2×10^4	1.6×10^4	3.7×10^4	3.2×10^4
0.5nm ALD-Ni-CZA40	6.1×10^4	2.5×10^4	2.3×10^4	1.4×10^4
0.5nm ALD-Ni-CZA40 used[1]	--	--	2.4×10^4	1.7×10^4

[1] 130 h TOS under DRM conditions

Comparing the rate constants between the low conversion RWGS and DRM TGA/DSC runs shows that for Ni-CZA40 k_{DRM} is within 15% of k_{RWGS} at 750°C, while at 650°C k_{RWGS} is 50% higher. On the other hand, the 0.5nm ALD-Ni-CZA40 has a 63% larger k_{DRM} at 750°C, and even at 650°C it is 44% larger. It is generally true for any catalyst capable of RWGS the ratio

k_{DRM}/k_{RWGS} will decrease as temperature decreases. But the addition of the Al_2O_3 overlayer did decrease, significantly, in absolute terms the RWGS rate constant, and this is consistent with the H_2/CO ratios seen in the bench scale reactor testing.

Figure 3.6 shows the XRD analysis of used 0.5nm ALD-Ni-CZA40, taken from the bench-scale reactor. No peaks are seen around 26.5° 2θ, indicating a lack of semi-graphitic or graphitic carbon on the used catalyst. The peak at 44.4° is difficult to assign. Unlike the uncoated sample where only Ni^0 was found (both primary peaks for Ni^0 were present), the single small peak at 44.4° for the used sample could arise from Ni^0, NiO, or γ-Al_2O_3. But the higher (than Ni) wt% of Al_2O_3 present here suggests that it arises from an Al_2O_3 phase. The CeO_2 crystallite sizes were calculated (using the Scherrer equation) to be 6.7 nm for the fresh and 6.4 nm for the used 0.5nm ALD-Ni-CZA40 samples based on the (111) reflection. The BET surface area and pore volume also showed little change upon use (fresh 72 m^2/g and 0.61 cm^3/g, used 77 m^2/g and 0.54 cm^3/g), but these changes do suggest some pore filling by solid material (probably coke) took place during the catalytic reaction.

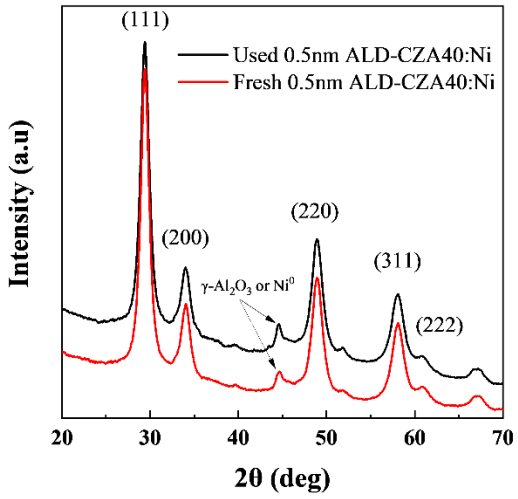

Figure 3.6. XRD spectrum of used (red) and fresh (black) 0.5nm ALD-Ni-CZA40.

XPS was used to explore the oxidation state of Ce in Ni-CZA40, and fresh and used 0.5nm ALD-Ni-CZA40. The Ce 3d spectra show multiple bands in the range of 880-920 eV due to O 2p valence band – Ce 4f hybridization. The deconvolution of the Ce 3d spectra results in 10 bands, 6 of which correspond with the Ce^{4+} state: v (884.8 eV), v'' (891.07 eV), v''' (898.4 eV), u (903.2 eV), u'' (909.55 eV), u''' (918.44).The remaining 4 bands correspond to the Ce^{3+} state: v_0 (881.4 eV), v' (887.71 eV), u_0 (900.32 eV), u' (906.27 eV).[5, 78, 83] The fraction of surface Ce^{3+} was calculated using equation 3.2.

$$Ce^{3+}\% = \frac{A_{Ce^{3+}}}{A_{Ce^{3+}} + A_{Ce^{4+}}} \qquad \text{Eq 3.2}$$

Where $A_{Ce}{}^{3+}$ and $A_{Ce}{}^{4+}$ are the sums of the areas of the Ce^{3+} and Ce^{4+} peaks listed above.[84] The spectra and the deconvolutions applied are shown in Figure 3.7. The spectra of the Ni-CZA40 and the fresh 0.5nm ALD-Ni-CZA40 catalysts are similar with both having a calculated Ce^{3+}% of 35%. The used 0.5nm ALD-Ni-CZA40 shows a reduction in the 884.7 (v) band intensity,

while increasing intensities are seen at 900.8 (u_0) and 905.95 (u'). The Ce^{3+}% for used 0.5nm ALD-Ni-CZA40 is 71%, a factor of two increase over the fresh catalyst. It is commonly observed that Ce-based catalysts used under reducing conditions exhibit an increase in Ce^{3+}.[85, 86] The amount of Ce^{3+} corresponds with the number of O-vacancies, thus a larger Ce^{3+}% means a larger number of O-vacancies present.[83, 84, 87] A large amount of O-vacancies is also associated with better coke resistance in Ni/CeO_2 DRM catalysts[5, 26, 40, 49]. This agrees with the reactor testing results. The Ce^{3+} numbers should be taken as relative only, due to the potential for XPS irradiation to create additional Ce^{4+} reduction, but the exact magnitude of this machine-dependent reduction is unknown.[88]

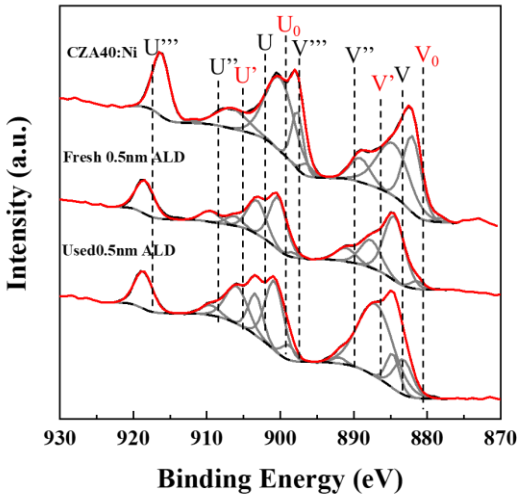

Figure 3.7. Ce 3d XPS spectrum of Ni-CZA40, used and fresh 0.5nm ALD- Ni-CZA40.

XANES was used to determine the oxidation state of the Ni in the same three catalysts as used for XPS. The Ni K-edge XANES for these three catalysts are shown in Figure 3.8a. The fresh and used ALD samples show little to no evidence of reduced Ni. The used ALD catalyst did lose peak intensity at the peak maximum of 8351 eV when compared to its fresh counterpart,

suggesting either less electron donation from the Ni, or fewer Ni absorbers. The Ni present in the ALD samples exists in the Ni^{2+} state but there are subtle differences between these XANES spectra and that of the NiO standard. In comparison, the fresh Ni-CZA40 shows the presence of some Ni^0, but still is mostly Ni^{2+} as evident from the white line position at 8351 eV which is more characteristic of Ni^{2+}. Linear combination fitting was done on all three catalysts. The fitting suggested that the uncoated Ni-CZA40 was ~34% Ni^0, while the other two samples were 0% Ni^0.

EXAFS analyses were performed to further explore the coordination environment around the Ni^{2+}. The analyses of ALD-coated samples present a difficult challenge due to the non-homogeneous nature of the overcoated system. While EXAFS fitting of Ni-CZO systems is widely documented[61, 78], the addition of the overlayer and the 2+ charge on the Ni presents extra layers of complexity due to the unknown positions of the Ni^{2+} atoms in either Al_2O_3, CeO_2, $CeAlO_3$, or as a pure-Ni containing phase such as $NiAl_2O_4$ or NiO. In particular γ-Al_2O_3 has two types of octahedral and one type of tetrahedral site, all of which can house vacancies into which Ni^{2+} could insert. To generate potential scattering pathway files in the Feff program, ATOMS files containing the positions of the atoms and the bond lengths for all of the above phases were obtained from XRD data, and then a single Ni core absorber was substituted for a cation in these files, except for $NiAl_2O_4$ and NiO, where the Ni atoms were already present.[89-92] The numbers of oxygen atoms were adjusted to maintain electroneutrality by removing an O-atom within the scattering volume, which consisted of a sphere of radius 5 Å from the core absorber.

Of all the possible phases listed above, none gave reasonable fits (as determined from the relative standard deviation of the FT-XAFS function, the R-value) other than NiO itself and Ni located in a tetrahedral γ-Al_2O_3 site. Figure 3.8b shows a fit to the bulk NiO lattice for both the fresh and used 0.5nm Al_2O_3 ALD-Ni-CZA40. The fit is not exact, but that is expected due to the

complex nature of the coated samples. It is unlikely that the Ni environment is pure bulk NiO, which would be inconsistent with the XRD results. The used sample shows a better fit to NiO than the fresh sample, the R-factor being 0.093 for the used and 0.143 for the fresh sample. This suggests a coordination environment more populated by Ni and O atoms in the used than fresh sample. Figure 3.8c shows the fits for Ni in a tetrahedral γ-Al_2O_3 site for both fresh and used 0.5nm ALD-Ni-CZA40. Just as with the case of fitting to NiO, the fit to a Ni-doped γ-Al_2O_3 is not exact. The fits for Ni substitution in an octahedral γ-Al_2O_3 site are similar but slightly worse.

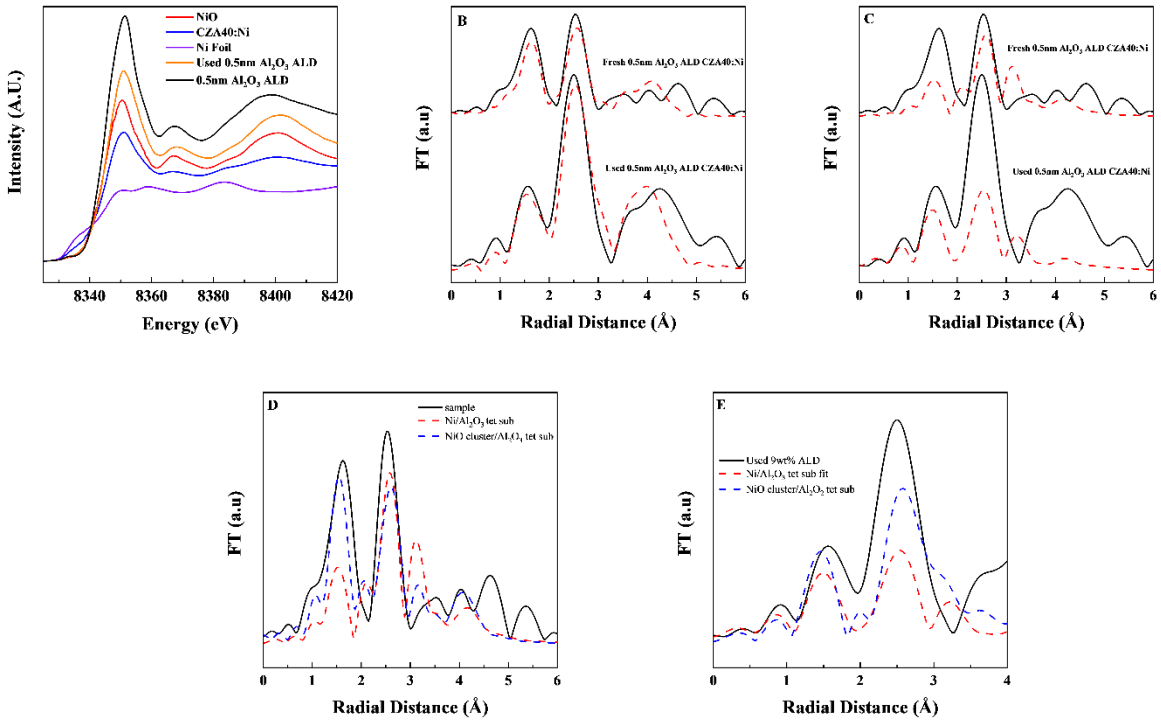

Figure 3.8. a.) Ni K-edge XANES for Ni-CZA40, fresh and used 0.5nm ALD-Ni-CZA40 b.) Fourier-transformed (FT) XAFS for fresh and used 0.5nm ALD-Ni-CZA40 (solid curves) compared to simulated curves for bulk NiO (dotted) c.) FT XAFS, same catalysts (solid curves), compared to simulated FT XAFS (dotted curves) for single atom Ni tetrahedral site substitution in γ-Al_2O_3. d.) FT XAFS of fresh 0.5nm ALD-Ni-CZA40 (solid curve) compared to simulated (dotted) curves for a single and dual ("cluster") Ni tetrahedral site substitution in γ-Al_2O_3. e.) FT XAFS of used 0.5nm ALD-Ni-CZA40 (solid curve) compared to simulated (dotted) curves for single and dual ("cluster") Ni tetrahedral site substitution in γ-Al_2O_3.

From both types of fits the nature of the peak at 1.5Å can be ascribed to first-shell O-atom scattering. The nature of the peak at 2.5Å cannot be so easily determined due to potential scattering from Ni, Al or Ce atoms, all of which could be located near 2.5 Å radial distance. To help determine the nature of this peak a new ATOMS file based on γ-Al_2O_3 was constructed with a second Ni atom placed in a tetrahedral site adjacent to the Ni core absorber. Electroneutrality

was again maintained by removing oxygen atoms as necessary. The comparisons for both the fresh and used 0.5nm ALD-Ni-CZA40 samples to Feff simulations of both the single and dual Ni-atom substituted γ-Al_2O_3 are seen in Figs 3.8d-e. It is seen that the dual-Ni atom substitution simulations better conform to the experimental FT XAFS data. The R-factors of the two samples for the regressions to these simulations decrease by roughly half (Table 3.3) when adding the second Ni atom to the lattice. It is evident that additional Ni atoms could be added at either tetrahedral or octahedral sites, and this would probably lower the R-factors further and improve the fits, but the number of possible permutations in Ni siting as the number of Ni atoms in Al_2O_3 cation vacancies increases becomes almost infinite. The primary results obtained from this exercise are that: (a) there is Ni-O clustering; and (b) that the clustering is likely situated in the alumina overlayer and not in the Ce-Zr mixed oxide.

Table 3.3. R-factors of EXAFS fits for 0.5 nm ALD-Ni-CZA

Catalyst	R-factor: NiO	R-factor: Ni/Al_2O_3 tet site	R-factor: NiO cluster /Al_2O_3 tet site
0.5nm ALD-Ni-CZA40	0.143	0.439	0.199
0.5nm ALD-Ni-CZA40 used[1]	0.096	0.425	0.225

[1] 130 h TOS under DRM conditions

Dark-field STEM and EDX images of the fresh and used 0.5nm ALD-Ni-CZA40 samples were taken. In Figs. 3.9-3.10 the planes marked CeO_2 represent those of a 1:1 Ce:Zr mixed CZO with a distorted fluorite structure, as was seen in the XRD results. It is impossible to distinguish the (200) plane of cubic NiO (0.203nm) from the (220) plane of CZO (0.191 nm CeO_2, 0.186-0.192 nm for CZO), which makes it difficult to assign some of the fringes to either species, thus these fringes are described as either NiO or CeO_2 planes. Both planes are common in their

respective oxides. Planes with d-spacings around ~0.261 nm are assigned to a $CeAlO_3$ phase and are therefore evidence of Ce from the CZO mixing with the Al_2O_3 ALD overlayer. The θ-Al_2O_3 region suggests possible generation of this higher temperature Al_2O_3 from surface hot spots, but θ-Al_2O_3 is not structurally very different from γ-Al_2O_3. The DF STEM images illustrate the poorly crystalline environment that the Ni is in and suggests why it is difficult to get exact fits to model structures in EXAFS.

Figs 3.11-3.12 show EDX maps of both fresh and used 0.5nm ALD-Ni-CZA40. Both images are at a lower magnification to capture several possible Ni particles. The fresh sample (Fig 3.11) shows dispersed Ni and no segregation of Ce/Zr. The used sample (Fig 3.12) clearly lost some of its initially high Ni dispersion due to crystal ripening, but there are still many regions of dispersed Ni present. An average surface Ni particle size was obtained from the EDS images for both the fresh and used 0.5nm ALD Ni-CZA40 samples. From fresh to used the average particle size increased from 15.8 to 17.3 nm, which is consistent with a slight loss of Ni dispersion.

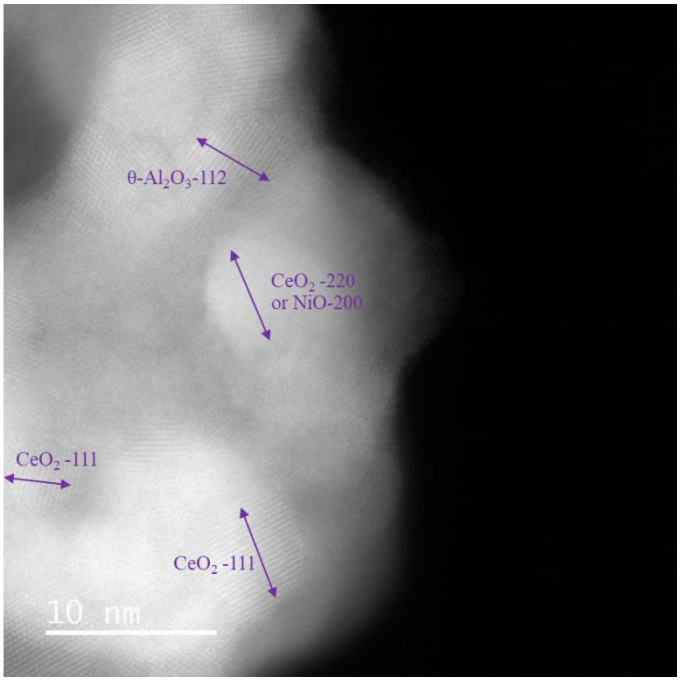

Figure 3.9. DF STEM of fresh 0.5nm Al_2O_3 ALD Ni-CZA40

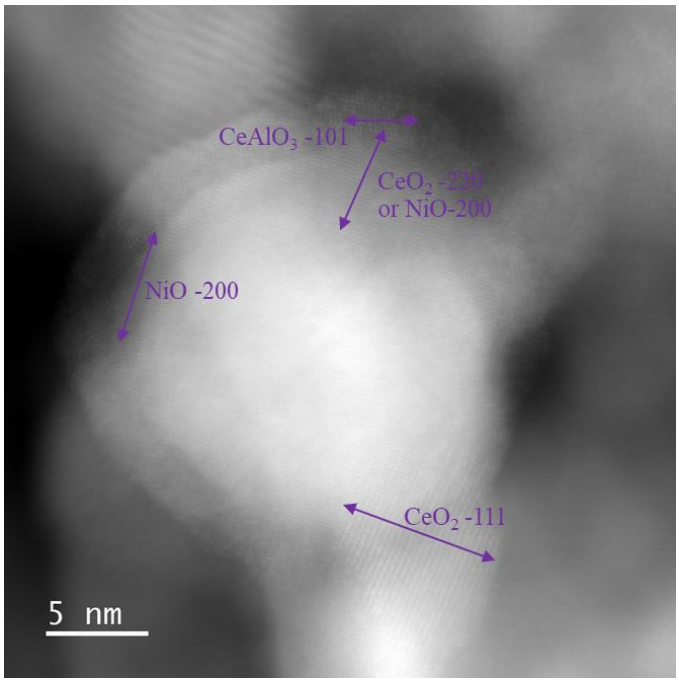

Figure 3.10. DF STEM of used 0.5nm Al_2O_3 ALD Ni-CZA40

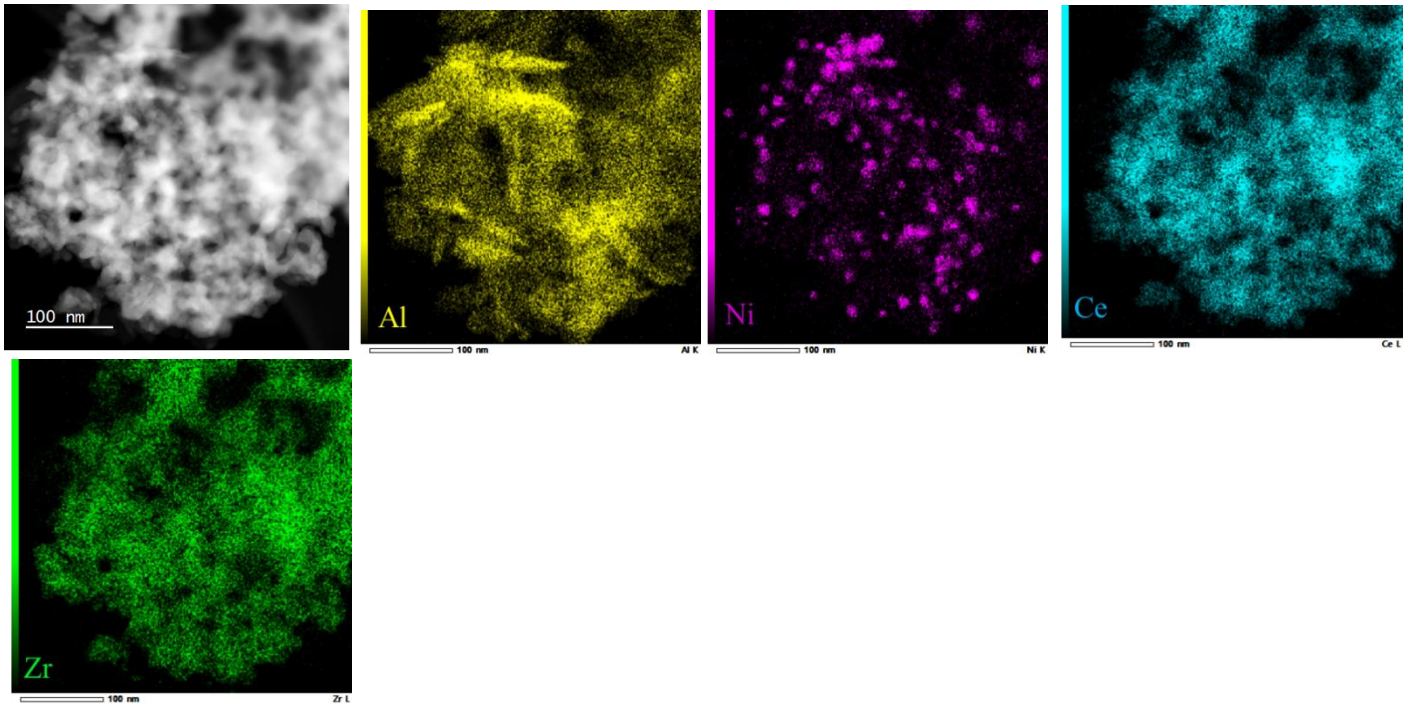

Figure 3.11. EDS mapping for a DF STEM image of fresh 0.5nm Al_2O_3 ALD Ni-CZA40.

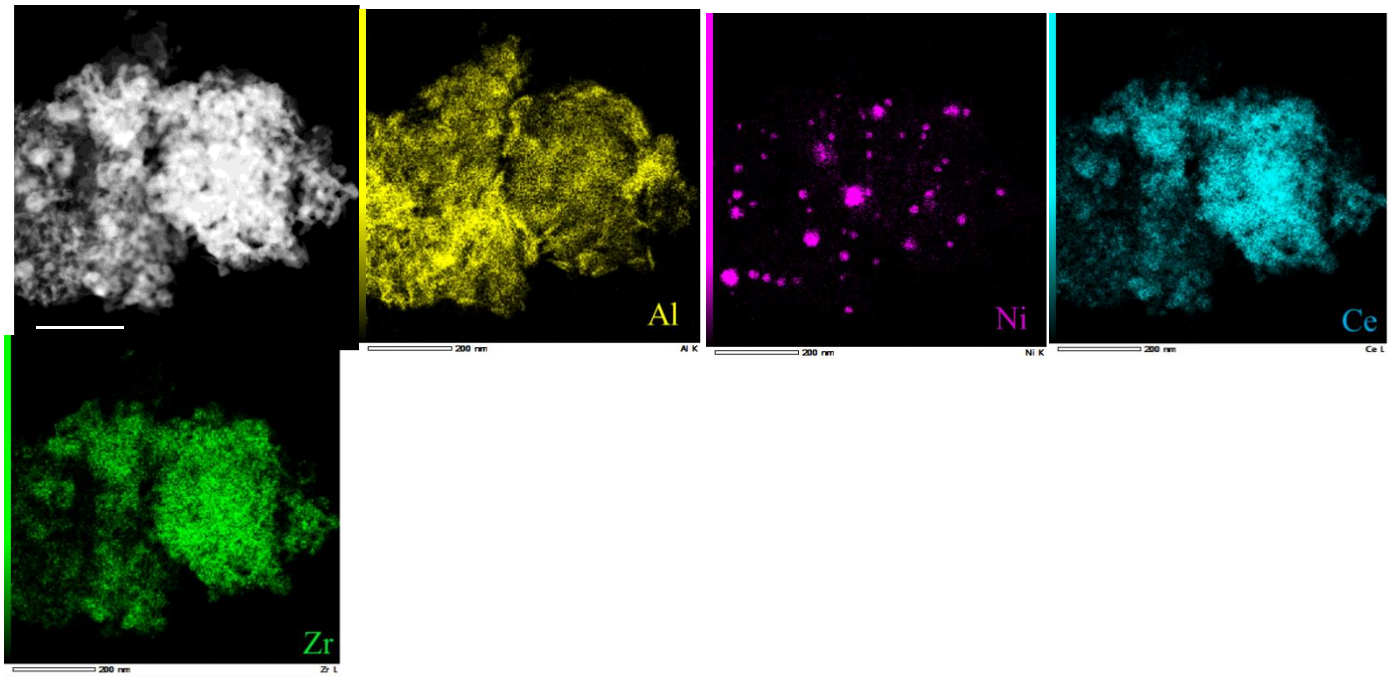

Figure 3.12. EDS mapping for a DF STEM image of used 0.5nm Al_2O_3 ALD Ni-CZA40.

Observations on the Kinetics

Earlier in this chapter there was a discussion of using the TGA/DSC as a screening tool to select the optimal catalyst that would then be tested further at higher conversion in a bench scale reactor. The forward rate constant for the DRM reaction was calculated from these TGA/DSC differential reactor data using a second order PFR model with volumetric expansion (equation 3.1). The rate constants were calculated and are shown in Table 3.2. The k_{DRM} for fresh ALD-Ni-CZA40 can be used in the same equation but with the other parameters charcteristic of DRM in a higher conversion reactor (W= 250 mg, F'= 150 mL/min, C_{a0} = 2.03 x 10^{-5} mol/mL). Doing so should predict the upper bound conversion in the bench scale reactor. It would be an upper bound because the reverse rate constant would have to be considered to predict a more realistic conversion.

However, the expected CH_4 conversion in the larger reactor using k_{DRM} from the TGA/DSC experiment for 0.5nm ALD-Ni-CZA40 is 53%, while the actual CH_4 conversion was 75%. This significant difference in expected vs. actual conversion demonstrates the magnitude of the sturctural change of the ALD-coated catalyst, which is evolving into a far more active state than what was initially put into the reactor. This is evident from the long induction period (Fig. 3.7) as well. Induction periods in Al_2O_3 ALD-coated catalysts have been observed before and are probably also associated with significant structural evolution.[21, 74]

Nature of the RWGS on ALD-coated Ni-CZA40

The analysis of the rate constants of DRM and RWGS is useful to gain insight into why the ALD-coated catalyst is more selective. With the uncoated Ni-CZA40, it was seen that the ratio k_{DRM}/k_{RWGS} at 750°C was slightly less than 1 while at 650°C is was well below 1. For the fresh 0.5nm ALD-Ni-CZA40 the ratios at 750°C and 650°C were both greater than 1, but the ratio decreased with temperature, which is generally true for any good RWGS catalyst. As previously stated both of these rate constants were obtained at conditions of equal partial pressures of the respective reactants for RWGS and DRM. For RWGS an equal ratio of partial pressures of H_2:CO_2 is somewhat of an oversimplication of the nature of these two reactants in the bench scale DRM system. In the bench scale system the H_2 and CO_2 concentrations vary greatly with reactor length. At the entrance of the reactor there is a lot of CO_2 but no H_2. Eventually both H_2 and CO_2 are present and can react to H_2O and CO by the RWGS reaction, although because of the stoichiometry of the DRM reaction they aren't likely to be equal in partial pressure. Further into the reactor, the reaction is less likely to happen because there is little CO_2. The ALD-coated catalyst exhibited two desireable behaviors, the first being a decreased k_{RWGS} reaction and the second being an increased k_{DRM}. The larger DRM rate constant means more CO_2 consumption, and as more CO_2 is consumed

the RWGS (which has an equilibrium constant of 0.48-0.76 over this temperature range) gradually reverses to the water-gas shift, regenerating H_2. Therefore the change in both rate constants in a favorable direction leads to the high H_2/CO ratio observed in the bench scale reactor results for 0.5nm ALD-Ni-CZA40.

Nature of surface Ni-Al-Ce interactions in DRM

Fully understanding the operando surface structure of the 0.5nm ALD-Ni-CZA40 catalyst or any other overcoated catalyst is a difficult to impossible task. However, with the characterization data presented here, it is possible to make a hypothesis as to the oxidation state and coordination environment of the surface Ni, Ce, and Al. By looking at the K-edge Ni XANES and EXAFS we concluded that most if not all of the Ni was in a 2+ oxidation state, and from all the XAFS fits, and in particular by comparing FT XAFS fits for 2 vs. 1 Ni atoms inserted into a tetrahedral alumina site (Figs. 3.8d-e), we know that the most likely Ni coordination environment is a state of Ni^{2+}-O clustering within a mixed oxide lattice. The Ni is not exactly NiO due to the lack of a NiO phase in XRD (Fig. 3.6), and the propensity of bulk NiO to reduce to Ni^0 at DRM conditions.[93] Most of the Ni is embeded in this oxide lattice, which could be similar to a NiO-Al_2O_3 mixture or could be more like a NiO-Al_2O_3-CeO_2 mixture. While the tetrahedral site of alumina was used as the model, the fit is far from perfect (Figs. 3.8c-e). There must be other atoms (Ni or Ce) around the Ni core absorber that affect its scattering.

Ce XPS (Fig. 3.7) was done to analyze the electronic properties of Ce near the surface. As shown, on going from fresh to used 0.5nm ALD-Ni-CZA40 the XPS-determined Ce^{3+} concentration increased from 35% to 71%. This is consistent with CeO_2 that has been doped with a transition metal.[16, 25, 87, 94] By examining the results of Ni K-edge XANES/EXAFS results, the Ce XPS results, and the DF STEM results showing some evidence of a $CeAlO_3$ phase, it is

hypothesized that there was gradual migration of Ce into the alumina overlayer, that Ni is in proximity to this mixed Ce-Al oxide, and that this mixing is associated with the significant changes in DRM and RWGS kinetics observed in the first 1-2 days of reactor operation. CeO_2 and Al_2O_3 have a known propensity to mix (ultimately forming the $CeAlO_3$ phase) under elevated temperatures like those experienced during DRM.[95, 96]

Comparison of ALD CZA to other overcoated or core-shell DRM catalysts

Core-shell architectures are common in DRM. As mentioned in Chapter 1, these architectures are supposed to suppress deactivation mechanisms or in some cases increase the DRM activity at lower temperatures. While this work is based on the use of ALD to deposit an overlayer of a different oxide, it is important to realize that there are other ways to do this, and that these other methods can produce core-shell microstructures. Thus, it is important for the results in this chapter to be analyzed in context with both ALD-deposited and core-shell DRM catalysts. Table 3.4 presents the turnover frequency (TOF, defined here as the number of mols of CH_4 converted per second per mol Ni in the catalyst) on a Ni basis, the H_2/CO ratio, and the DRM temperature for the 0.5nm ALD-Ni-CZA40 along with some other core-shell catalysts. Catalysts with a TOF of 0.25 or better operating in the 700-800°C range with some proven long-range stability and with H_2/CO of >0.7 are arbitrarily chosen as promising DRM catalysts; there aren't many of these in the open literature. However, some other catalysts are included in Table 3.4 that don't meet these criteria, for comparison purposes.

It can be seen from Table 3.4 that the TOF of 0.5nm ALD-Ni-CZA40 is well below the TOF of another Al_2O_3 ALD catalyst (the third row of the table). However, this catalyst deactivated very fast, with a 20% loss of activity in 60 hours. By comparison, the 0.5nm ALD-Ni-CZA40 didn't lose activity through 130 h time onstream. The other ALD Al_2O_3 catalyst showed an

induction period similar to ours before maximum activity was achieved, and the induction period was attributed to the reduction of $NiAl_2O_4$ to separate phases of Ni^0 and Al_2O_3. However, this is not the case in our work because as seen there is no evidence of Ni^0 in 0.5nm ALD-Ni-CZA40.

Table 3.4. Turnover frequency (total Ni atom basis) and H_2/CO of core-shell type DRM catalysts

Catalyst (molar basis)	T °C	TOF s^{-1}	H_2/CO	Ref
0.5nm ALD-Ni-CZA40	750	0.28	0.98	This work
0.015Ni/0.025Mg/0.0062Al/ZrOx	800	1.94	0.78	[55]
Ni0.018/AlOx (ALD)	700	1.0	N/A	[21]
Ni0.018/AlOx/LaO_x (ALD)	700	1.0	N/A	[74]
Ni0.014/AlOx (ALD)	700	0.51	N/A	[73]
Ni0.038/Ce0.068/SiO_x	700	0.17	0.67	[56]
(core-shell)	750	0.39	0.89	
Ni0.023/SiO_x (core-shell)	750	0.27	0.87	[97]

Ahn et al. continued the work on ALD-type DRM catalysts (fourth row of the table) by adding La to the Al_2O_3 overlayer to fill cation vacancies in the γ-Al_2O_3. This was shown to eliminate the induction period seen before. However, this catalyst lost ~20% of the activity in ~40 h.

Tathod et al. developed a highly active Ni/$MgAl_2O_4$/Zr catalyst for DRM (second row of the table). While the activity of this catalyst is far superior to any known Ni-based DRM catalyst, it is important to realize a few details. First this catalyst is operating at a very high temperature of 800°C, where it is easier to attain high DRM activity, high H_2/CO ratio, and minimal coking just based on equilibrium considerations. But even at this highly favorable temperature the sample is far less selective (0.78 H_2/CO ratio) than the 0.5nm ALD-Ni-CZA40 catalyst. Finally, the Ni/$MgAl_2O_4$/Zr catalyst is less stable.

The Ce-based DRM core-shell catalysts have been quite popular due to the ability of an active CeO_x phase to enhance the activity of Ni-based catalysts, attributed to the formation of OVs formed by doping the CeO_x (with Ni, e.g.). These OVs are known to activite CO_2. Das et al

synthesized a Ni/SiO_2@CeO_2 core-shell material that was active at 700-750°C (sixth and seventh rows of the table). While its activity at 750°C was better than the activity of 0.5nm ALD-Ni-CZA40, the latter is more selective by more than 10%.

Core-shell catalysts that are Ni@oxide have been studied as well. Han et al. coated Ni nanoparticles with a SiO_2 shell (last row of the table). This catalyst was approximately of same activity as 0.5nm ALD-Ni-CZA40 (0.28) and showed excellent stability, but was again less selective by more than 10%. For DRM, selectivity is far more important than raw activity, because H_2 is a far more valuable product than CO.

In summary, the results of the present work show that a ALD-deposited catalyst, made by overcoating Al_2O_3 on CeO_2-ZrO_2, compares well to other core-shell catalysts for DRM by all significant metrics. The mixture of a non-reducible and reducible support in a core-shell architecture with Ni initially sandwiched between them is a promising path to achieving both highly active, selective and stable DRM catalysts, although even longer term stability would need to be evaluated.

Chapter 4. Conclusions and Future Work

In summary, ALD coatings were applied to a Ni/CZO system using a standard alumina ALD method to study the effect of a non-reducible overcoat on the DRM catalytic activity, catalytic lifetime, and H_2/CO ratio. Application of a 0.5 nm thick Al_2O_3 shell showed an improvement in all three of the desired catalyst metrics, with an ~1 H_2/CO ratio achieved. The stability and selectivity of the 0.5 nm ALD coated sample compares well to other core-shell Ni DRM catalysts. The application of an ALD overlayer increased the lifetime of the CZA40:Ni catalyst by 10-fold. Kinetics studies of the affect of the Al_2O_3 overlayer showed that both a decrease in the RWGS constant and an increase in the DRM rate constant led to an ~1 H_2/CO ratio for the 0.5nm ALD-Ni-CZA40 catalyst. The application of an overlayer reduced sintering possibly because Ni was shown to be less reducible. It is possible that the long induction time seen during bench scale reactor testing is associated with Ce migration from the bulk CZO to the surface and a mixed CeO_2-Al_2O_3 phase was made. Additionally, it is likely that this mixed oxide is where the Ni^{2+} observed in the XAS experiments is located.

Future work will need to focus on the changes in the catalyst sturcture with DRM time on stream. By performing *in situ* XAS we can observe how the Ni K-edge and Ce L-edge energies change to obtain a fuller picture. Using these results we can better design the ALD coated samples to obtain highly active and selective catalysts from the start of reaction instead of needing to wait ~50 h. In particular, if the highly active phase is Ni in a CeO_2-Al_2O_3 mixed oxide then the application of a CeO_2 ALD shell to a Ni/Al_2O_3 will need to be tested. It is also important to attempt DRM at temperatures lower than 750°C for technoeconomic reasons. However, this region of temperature is known to enhance the primary coke formation reaction (the Boudouard reaction) as

well as the RWGS. Application of a reducable overlayer to other supported Ni on non-reducible oxide catalysts could result in a more optimal core-shell system for DRM at lower temperatures.

Appendix A. Experimental Procedures – Reactor Testing

A.1 Reactor operating procedure

1. Load catalyst from the bottom. Fill bottom and top of reactor with α-Al_2O_3 and quartz wool.
2. Purge the system with N_2 at least for 10 min.
3. Bring the reactor temperature to the target, and all feed and product lines above 100°C.
4. Pretreat the sample with either N_2, 5% H_2/N_2 or air overnight.
5. Purge the system with N_2 for at least 10 min.
6. Bring the reactor temperature to the operating temperature.
7. Switch from N_2 to the reaction feed. Gas flows are controlled and measured by the mass flow controllers, with flow rates recorded using the LabVIEW software. The total outlet flow rates were measured by bubble meter.
8. Set up a GC sequence to take samples automatically.
9. Switch the reacting gases to N_2 after the experiment is finished. Lower the temperature for the reactor and feed/product lines

A.2 Gas Chromatographic Analysis

The gas samples taken after the reactor were analyzed by an Agilent 6890N GC/MS. Three 1/8" molecular sieve packed columns, Wasson K1 (6 ft), K2 (7 ft), and K2S (2 ft) in series were used to separate hydrogen from the rest of the gaseous mixture, with the H_2 analyzed by a thermal conductivity detector. A 1 mL sample was injected using N_2 as the carrier gas. A pressure regulator set at 30 psig controlled the flow of carrier gas in the columns. Another 1 mL sample was injected into a 0.53 mm, 50 m capillary column (Wasson KC080) to separate N_2, CO, CO_2, CH_4 and water, also analyzed by a thermal conductivity detector. Helium was the carrier gas, controlled by the back inlet electronic flow controller. A third sample was injected (as needed) to a 100 m, 0.25 mm Wasson KC066 column which separated all components and fed the MSD, which was used for

qualitative confirmation of the components. Helium was the carrier gas, controlled by the front inlet electronic flow controller. The oven program and TCD details are provided below. GC calibration factors and retention times are presented in Table A1.

Front Inlet – Split; 120°C; P: 4.5 psi; column flow 0.5 mL/min; total flow: 7.8 mL/min; split ratio = 10:1; split flow = 4.8 mL/min

Back Inlet – Split; 120°C; P: 7.4 psi; column flow 5.4 mL/min; total flow: 79 mL/min; split ratio = 13.1:1; split flow=70.4 mL/min 78

Front Detector – TCD; 200°C; 16.5 mL/min ref. flow; 11 mL/min makeup flow; Gas = He

Back Detector – TCD; 200°C; 20 mL/min ref. flow; 3 mL/min makeup flow; Gas = N2; Negative polarity

GC Oven Program – Initial Temp = 30°C; Initial time = 7 min; Rate1 = 10°C/min to 100°C; 5 min hold; Rate2 = 10°C/min to 130°C; 16 min hold Post Temp= 30°C;

Post Time = 15 min; Total run time = 38 min

Packed Column Auxiliary Oven Temperature Program – Initial Temp = 50°C; Initial time = 5 min; Rate1 = 10°C/min to 120°C, hold 11 min; Rate2 = 10°C/min to 50°C Chase heater – 100°C Injector (GSVs) oven – 200°C

Table A.1 GC Calibration Factors and Rentention Times

Component	GC Factor Mol (μmol)/area (MM)[1]	Rentention Time (min)
CO	0.46	3.6
CO_2	0.44	8.9
N_2	0.37	3.5
CH_4	0.69	4.3
H_2O	0.55	21.3
H_2	0.082	2.8[2]

[1]These are the final GC factors. The system has been re-calibrated three times in six years.
[2]This is the retention time for the packed columns.

Appendix B. Data Processing Details for XPS, XANES, and EXAFS

B.1. XPS

XPS data processing was performed with CasaXPS, version 2.3.25. The Shirley background subtraction and Gaussian/Lorentzian peak shapes were applied during the peak fitting. A 70% Gaussian/30% Lorentzian peak shape was used. The binding energies for all spectra were calibrated using the adventitious C1s peak at 284.4 eV.

B.2 XANES and EXAFS

B.2.1 XANES Data Processing

The XANES data processing was performed using Athena 0.9.061. Normalization is controlled by the value of E_0 (edge energy) and the pre-edge and normalization range. E_0 is determined by the maximum of the 1st derivative of the spectral data. The pre-edge range was set to -150 to -20 eV relative to E_0. Normalization range is >150 eV beyond E_0. After the spectra are deglitched and normalized they are merged to get a better estimate of the white line and signal to noise ratio. Background subtraction is controlled by the Rbkg parameter, which was set to 1-1.3 depending on the spectra, to eliminate spurious peaks at low R-values.

B.2.2 EXAFS Fitting

XAFS fitting was performed in Artemis 0.9.26. ATOMS was used to generate input files for Feff calculation. The output Feff file contains the detailed structural information such as the atomic coordination numbers, effective path lengths, and geometry of the scattering paths.

The EXAFS spectrum is defined by the EXAFS equation, which is written as a sum of the contributions for all scattering paths. Each scattering path is described by the equation written as follows:

$$\chi_i(k) \equiv \frac{(N_i S_0^2) F_{effi}(k)}{kR_i^2} \sin[2kR_i + \varphi_i(k)] e^{-2\sigma_i^2 k^2} e^{\frac{-2R_i}{\lambda(k)}}$$

Three parameters were varied to obtain the best possible fits of the Ni K-edge data, σ^2 (Debye-Waller factor), ΔE_0 (deviation in E_0 caused by structural deviations from the ideal crystal structure), and ΔR (deviation in the interatomic distance). The parameter S_0^2 (amplitude reduction factor) was obtained from a single Ni standard, bulk NiO, and was assumed constant for all scattering paths. The coordination numbers (N) were constrained to the ideal values for the proposed theoretical structure.

The Debye-Waller factors for multple scattering paths were estimated as follows.

Double scattering: S1S2 = 1.5*ss

3-leg (triangle): S1S2 = 0.5*ss_ssa

Non-forward linear: S1S1 = ss2

Forward through absorber: S1+S1 = 2*ss

Rattle: S1+S1 = 4*ss

where ss is the Debye-Waller factor of the primary scatterer, and ssa is the Debye-Waller factor of the next nearest atom.

The confidence limits on all fitted parameters are given by the program. Artemis uses the R-factor (the residual standard deviation) as a goodness of fit parameter. It is defined as follows:

$$R - factor = \frac{\sum_i (data_i - fit_i)^2}{\sum_i data_i^2}$$

Each fit was iterated by varying a group of the regression parameters until no further decrease in R-factor was found. The fitting results for all fits performed are shown below in Tables b.1-b.5

Table B.1 Fitting Results using NiO

Sample	State	Shell	N	σ^2 (Å^2)	R (Å)	R-factor
0.5nm Al_2O_3 CZA40:Ni-PR	Fresh	1st Ni-O	6	0.00573	2.07363	0.143
		1st Ni-Ni	12	0.01257	2.9475	
		2nd Ni-O	8	0.00573	3.59933	
		2nd Ni-Ni	6	0.01257	4.20697	
		3rd Ni-O	24	0.00573	4.64983	
0.5nm Al_2O_3 CZA40:Ni-PR	used	1st Ni-O	6	0.00273	2.08313	0.096
		1st Ni-Ni	12	0.00469	2.95528	
		2nd Ni-O	8	0.00273	3.60883	
		2nd Ni-Ni	6	0.00469	4.17618	
		3rd Ni-O	24	0.00273	4.65933	

Table B.2 Fitting Results using Ni/CeO_2

Sample	State	Shell	N	σ^2 (Å^2)	R (Å)	E0 (eV)	R-factor
0.5nm Al_2O_3 CZA40:Ni-PR	Fresh	1st Ni-O	8	0.0063	2.00679	-13.446	0.393
		1st Ni-Ce	12	0.01197	3.65142		
		2nd Ni-O	24	0.0063	4.4855		
0.5nm Al_2O_3 CZA40:Ni-PR	used	1st Ni-O	8	0.00235	2.3425	28.813	0.565
		1st Ni-Ce	12	0.00089	4.27289		
		2nd Ni-O	24	0.00235	4.80727		

Table B.3 Fitting Results using Ni in an octahedral site, γ-Al_2O_3

Sample	State	Shell	N	σ^2 (Å^2)	R (Å)	E0 (eV)	R-factor
0.5nm Al_2O_3 CZA40:Ni-PR	Fresh	1st Ni-O	6	0.00483	2.05247	-1.065	0.2345
		1st Ni-Al	5	0.00729	2.8066		
		2nd Ni-Al	5	0.00729	3.2666		
		2nd Ni-O	2	0.00483	3.4646		
		3rd Ni-O	6	0.00483	3.5892		
		4th Ni-O	12	0.00483	4.5344		
		5th Ni-O	12	0.00483	4.6295		
		3rd Ni-Al	11	0.00729	4.8367		
0.5nm Al_2O_3 CZA40:Ni-PR	used	1st Ni-O	6	0.003	2.1088	3.424	0.382
		1st Ni-Al	5	0.003	2.7847		
		2nd Ni-Al	5	0.003	3.2691		
		2nd Ni-O	2	0.003	3.521		
		3rd Ni-O	6	0.003	3.6455		
		4th Ni-O	12	0.003	4.5908		
		5th Ni-O	12	0.003	4.6858		
		3rd Ni-Al	11	0.003	4.8392		

Table B.4 Fitting Results using Ni in a tetrahedral site, γ-Al_2O_3

Sample	State	Shell	N	σ^2 (Å^2)	R (Å)	E0 (eV)	R-factor
0.5nm Al_2O_3 CZA40:Ni-PR	Fresh	1st Ni-O	2	0.00247	2.0077	-8.638	0.439
		1st Ni-Al	12	0.00453	3.15704		
		2nd Ni-O	12	0.00247	3.50494		
		2nd Ni-Al	4	0.00453	3.30334		
		3rd Ni-O	12	0.00247	4.46104		
0.5nm Al_2O_3 CZA40:Ni-PR	used	1st Ni-O	4	0.003	2.04015	-6.972	0.425
		1st Ni-Al	12	0.003	3.1548		
		2nd Ni-O	12	0.003	3.5374		
		2nd Ni-Al	4	0.003	3.3011		
		3rd Ni-O	12	0.003	4.49345		

Table B.5 Fitting Results using a Ni cluster in tetrahedral sites, γ-Al_2O_3

Sample	State	Shell	N	σ^2 ($Å^2$)	R (Å)	E0 (eV)	R-factor
0.5nm Al_2O_3 CZA40:Ni-PR	Fresh	1st Ni-O	4	0.00149	1.9949	-8.092	0.199
		1st Ni-Al	12	0.00652	3.1682		
		2nd Ni-O	12	0.00149	3.4921		
		1st Ni-Ni	4	0.00652	3.3145		
		2nd Ni-Al	4	0.00247	3.3145		
0.5nm Al_2O_3 CZA40:Ni-PR	used	1st Ni-O	4	0.001	1.9934	-9.272	0.225
		1st Ni-Al	12	0.001	3.1425		
		2nd Ni-O	12	0.001	3.4905		
		1st Ni-Ni	4	0.001	3.2888		
		2nd Ni-Al	4	0.001	3.2888		

References

1. Liu, P. R.; Raftery, A. E., Country-based rate of emissions reductions should increase by 80% beyond nationally determined contributions to meet the 2 degrees C target. *Commun Earth Environ* **2021,** *2*.

2. den Elzen, M.; Kuramochi, T.; Höhne, N.; Cantzler, J.; Esmeijer, K.; Fekete, H.; Fransen, T.; Keramidas, K.; Roelfsema, M.; Sha, F.; van Soest, H.; Vandyck, T., Are the G20 economies making enough progress to meet their NDC targets? *Energy Policy* **2019,** *126*, 238-250.

3. Whipple, D. T.; Kenis, P. J. A., Prospects of CO2 Utilization via Direct Heterogeneous Electrochemical Reduction. *The Journal of Physical Chemistry Letters* **2010,** *1* (24), 3451-3458.

4. Saravanan, A.; Senthil kumar, P.; Vo, D.-V. N.; Jeevanantham, S.; Bhuvaneswari, V.; Anantha Narayanan, V.; Yaashikaa, P. R.; Swetha, S.; Reshma, B., A comprehensive review on different approaches for CO2 utilization and conversion pathways. *Chemical Engineering Science* **2021,** *236*.

5. Safavinia, B.; Wang, Y.; Jiang, C.; Roman, C.; Darapaneni, P.; Larriviere, J.; Cullen, D. A.; Dooley, K. M.; Dorman, J. A., Enhancing CexZr1–xO2 Activity for Methane Dry Reforming Using Subsurface Ni Dopants. *ACS Catalysis* **2020,** *10* (7), 4070-4079.

6. Shen, L.; Xu, J.; Zhu, M.; Han, Y.-F., Essential Role of the Support for Nickel-Based CO2 Methanation Catalysts. *ACS Catalysis* **2020,** *10* (24), 14581-14591.

7. Ma, J.; Sun, N.; Zhang, X.; Zhao, N.; Xiao, F.; Wei, W.; Sun, Y., A short review of catalysis for CO2 conversion. *Catalysis Today* **2009,** *148* (3-4), 221-231.

8. Artz, J.; Muller, T. E.; Thenert, K.; Kleinekorte, J.; Meys, R.; Sternberg, A.; Bardow, A.; Leitner, W., Sustainable Conversion of Carbon Dioxide: An Integrated Review of Catalysis and Life Cycle Assessment. *Chem Rev* **2018,** *118* (2), 434-504.

9. Vogt, C.; Kranenborg, J.; Monai, M.; Weckhuysen, B. M., Structure Sensitivity in Steam and Dry Methane Reforming over Nickel: Activity and Carbon Formation. *ACS Catalysis* **2019,** *10* (2), 1428-1438.

10. Song, Y.; Ozdemir, E.; Ramesh, S.; Adishev, A.; Subramanian, S.; Harale, A.; Albuali, M.; Fadhel Bandar, A.; Jamal, A.; Moon, D.; Choi Sun, H.; Yavuz Cafer, T., Dry reforming of methane by stable Ni–Mo nanocatalysts on single-crystalline MgO. *Science* **2020,** *367* (6479), 777-781.

11. Bengaard, H. S.; Nørskov, J. K.; Sehested, J.; Clausen, B. S.; Nielsen, L. P.; Molenbroek, A. M.; Rostrup-Nielsen, J. R., Steam Reforming and Graphite Formation on Ni Catalysts. *Journal of Catalysis* **2002,** *209* (2), 365-384.

12. Dooley, K., Personal Communication. Cain Department of Chemical Engineering, Louisiana State University, Baton Rouge, LA, August 2022.

13. Abdullah, B.; Abd Ghani, N. A.; Vo, D.-V. N., Recent advances in dry reforming of methane over Ni-based catalysts. *Journal of Cleaner Production* **2017,** *162*, 170-185.

14. Zhang, Z.; Verykios, X. E.; MacDonald, S. M.; Affrossman, S., Comparative Study of Carbon Dioxide Reforming of Methane to Synthesis Gas over Ni/La2O3 and Conventional Nickel-Based Catalysts. *The Journal of Physical Chemistry* **1996,** *100* (2), 744-754.

15. Mette, K.; Kühl, S.; Tarasov, A.; Willinger, M. G.; Kröhnert, J.; Wrabetz, S.; Trunschke, A.; Scherzer, M.; Girgsdies, F.; Düdder, H.; Kähler, K.; Ortega, K. F.; Muhler, M.; Schlögl, R.; Behrens, M.; Lunkenbein, T., High-Temperature Stable Ni Nanoparticles for the Dry Reforming of Methane. *ACS Catalysis* **2016,** *6* (10), 7238-7248.

16. Jiang, C.; Akkullu, M. R.; Li, B.; Davila, J. C.; Janik, M. J.; Dooley, K. M., Rapid screening of ternary rare-earth – Transition metal catalysts for dry reforming of methane and characterization of final structures. *Journal of Catalysis* **2019,** *377*, 332-342.

17. Vasiliades, M. A.; Djinović, P.; Pintar, A.; Kovač, J.; Efstathiou, A. M., The effect of CeO2–ZrO2 structural differences on the origin and reactivity of carbon formed during methane dry reforming over NiCo/CeO2–ZrO2 catalysts studied by transient techniques. *Catalysis Science & Technology* **2017,** *7* (22), 5422-5434.

18. Lyu, Y.; Jocz, J.; Xu, R.; Stavitski, E.; Sievers, C., Nickel Speciation and Methane Dry Reforming Performance of Ni/CexZr1–xO2 Prepared by Different Synthesis Methods. *ACS Catalysis* **2020,** *10* (19), 11235-11252.

19. Yang, X.; Li, Q.; Lu, E.; Wang, Z.; Gong, X.; Yu, Z.; Guo, Y.; Wang, L.; Guo, Y.; Zhan, W.; Zhang, J.; Dai, S., Taming the stability of Pd active phases through a compartmentalizing strategy toward nanostructured catalyst supports. *Nat Commun* **2019,** *10* (1), 1611.

20. Guo, J.; Lou, H.; Zhao, H.; Chai, D.; Zheng, X., Dry reforming of methane over nickel catalysts supported on magnesium aluminate spinels. *Applied Catalysis A: General* **2004,** *273* (1), 75-82.

21. Littlewood, P.; Liu, S.; Weitz, E.; Marks, T. J.; Stair, P. C., Ni-alumina dry reforming catalysts: Atomic layer deposition and the issue of Ni aluminate. *Catalysis Today* **2020,** *343*, 18-25.

22. Ziemba, M.; Schilling, C.; Ganduglia-Pirovano, M. V.; Hess, C., Toward an Atomic-Level Understanding of Ceria-Based Catalysts: When Experiment and Theory Go Hand in Hand. *Acc Chem Res* **2021,** *54* (13), 2884-2893.

23. Bunluesin, T.; Gorte, R. J.; Graham, G. W., Studies of the water-gas-shift reaction on ceria-supported Pt, Pd, and Rh: Implications for oxygen-storage properties. *Applied Catalysis B: Environmental* **1998,** *15* (1), 107-114.

24. Duprez, D.; Descorme, C.; Birchem, T.; Rohart, E., Oxygen Storage and Mobility on Model Three-Way Catalysts. *Topics in Catalysis* **2001,** *16* (1), 49-56.

25. Löfberg, A.; Guerrero-Caballero, J.; Kane, T.; Rubbens, A.; Jalowiecki-Duhamel, L., Ni/CeO 2 based catalysts as oxygen vectors for the chemical looping dry reforming of methane for syngas production. *Applied Catalysis B: Environmental* **2017,** *212*, 159-174.

26. Laosiripojana, N.; Assabumrungrat, S., Methane steam reforming over Ni/Ce–ZrO2 catalyst: Influences of Ce–ZrO2 support on reactivity, resistance toward carbon formation, and intrinsic reaction kinetics. *Applied Catalysis A: General* **2005,** *290* (1), 200-211.

27. Liu, Z.; Lustemberg, P.; Gutierrez, R. A.; Carey, J. J.; Palomino, R. M.; Vorokhta, M.; Grinter, D. C.; Ramirez, P. J.; Matolin, V.; Nolan, M.; Ganduglia-Pirovano, M. V.; Senanayake, S. D.; Rodriguez, J. A., In Situ Investigation of Methane Dry Reforming on Metal/Ceria(111) Surfaces: Metal-Support Interactions and C-H Bond Activation at Low Temperature. *Angew Chem Int Ed Engl* **2017,** *56* (42), 13041-13046.

28. Tsukuma, K.; Shimada, M., Strength, fracture toughness and Vickers hardness of CeO2-stabilized tetragonal ZrO2 polycrystals (Ce-TZP). *Journal of Materials Science* **1985,** *20* (4), 1178-1184.

29. Fornasiero, P.; Balducci, G.; Di Monte, R.; Kašpar, J.; Sergo, V.; Gubitosa, G.; Ferrero, A.; Graziani, M., Modification of the Redox Behaviour of CeO2Induced by Structural Doping with ZrO2. *Journal of Catalysis* **1996,** *164* (1), 173-183.

30. Montini, T.; Melchionna, M.; Monai, M.; Fornasiero, P., Fundamentals and Catalytic Applications of CeO2-Based Materials. *Chem Rev* **2016,** *116* (10), 5987-6041.

31. Kambolis, A.; Matralis, H.; Trovarelli, A.; Papadopoulou, C., Ni/CeO2-ZrO2 catalysts for the dry reforming of methane. *Applied Catalysis A: General* **2010,** *377* (1-2), 16-26.

32. Hirano, M.; Suda, A., Oxygen Storage Capacity, Specific Surface Area, and Pore-Size Distribution of Ceria–Zirconia Solid Solutions Directly Formed by Thermal Hydrolysis. *Journal of the American Ceramic Society* **2003,** *86* (12), 2209-2211.

33. Shah, P. R.; Kim, T.; Zhou, G.; Fornasiero, P.; Gorte, R. J., Evidence for Entropy Effects in the Reduction of Ceria−Zirconia Solutions. *Chemistry of Materials* **2006,** *18* (22), 5363-5369.

34. Bulfin, B.; Call, F.; Vieten, J.; Roeb, M.; Sattler, C.; Shvets, I. V., Oxidation and Reduction Reaction Kinetics of Mixed Cerium Zirconium Oxides. *The Journal of Physical Chemistry C* **2016,** *120* (4), 2027-2035.

35. Kim, D.-J., Lattice Parameters, Ionic Conductivities, and Solubility Limits in Fluorite-Structure MO2 Oxide [M = Hf4+, Zr4+, Ce4+, Th4+, U4+] Solid Solutions. *Journal of the American Ceramic Society* **1989,** *72* (8), 1415-1421.

36. Ramírez-Cabrera, E.; Atkinson, A.; Chadwick, D., Catalytic steam reforming of methane over Ce0.9Gd0.1O2−x. *Applied Catalysis B: Environmental* **2004,** *47* (2), 127-131.

37. San-José-Alonso, D.; Juan-Juan, J.; Illán-Gómez, M. J.; Román-Martínez, M. C., Ni, Co and bimetallic Ni–Co catalysts for the dry reforming of methane. *Applied Catalysis A: General* **2009,** *371* (1), 54-59.

38. Jin, T.; Zhou, Y.; Mains, G. J.; White, J. M., Infrared and x-ray photoelectron spectroscopy study of carbon monoxide and carbon dioxide on platinum/ceria. *The Journal of Physical Chemistry* **1987,** *91* (23), 5931-5937.

39. Staudt, T.; Lykhach, Y.; Tsud, N.; Skála, T.; Prince, K. C.; Matolín, V.; Libuda, J., Ceria reoxidation by CO2: A model study. *Journal of Catalysis* **2010,** *275* (1), 181-185.

40. Kim, D.; Stowe, K.; Muller, F.; Maier, W., Mechanistic study of the unusual catalytic properties of a new NiCe mixed oxide for the CO2 reforming of methane. *Journal of Catalysis* **2007,** *247* (1), 101-111.

41. Ang, M. L.; Oemar, U.; Saw, E. T.; Mo, L.; Kathiraser, Y.; Chia, B. H.; Kawi, S., Highly Active Ni/xNa/CeO2 Catalyst for the Water–Gas Shift Reaction: Effect of Sodium on Methane Suppression. *ACS Catalysis* **2014,** *4* (9), 3237-3248.

42. Goguet, A.; Meunier, F. C.; Tibiletti, D.; Breen, J. P.; Burch, R., Spectrokinetic Investigation of Reverse Water-Gas-Shift Reaction Intermediates over a Pt/CeO2 Catalyst. *The Journal of Physical Chemistry B* **2004,** *108* (52), 20240-20246.

43. Zhu, Y.-A.; Chen, D.; Zhou, X.-G.; Yuan, W.-K., DFT studies of dry reforming of methane on Ni catalyst. *Catalysis Today* **2009,** *148* (3), 260-267.

44. Pan, Y.; Liu, C.-j.; Ge, Q., Adsorption and Protonation of CO2 on Partially Hydroxylated γ-Al2O3 Surfaces: A Density Functional Theory Study. *Langmuir* **2008,** *24* (21), 12410-12419.

45. Horiuchi, T.; Hidaka, H.; Fukui, T.; Kubo, Y.; Horio, M.; Suzuki, K.; Mori, T., Effect of added basic metal oxides on CO2 adsorption on alumina at elevated temperatures. *Applied Catalysis A: General* **1998,** *167* (2), 195-202.

46. Quindimil, A.; De-La-Torre, U.; Pereda-Ayo, B.; Davó-Quiñonero, A.; Bailón-García, E.; Lozano-Castelló, D.; González-Marcos, J. A.; Bueno-López, A.; González-Velasco, J. R., Effect of metal loading on the CO2 methanation: A comparison between alumina supported Ni and Ru catalysts. *Catalysis Today* **2020,** *356*, 419-432.

47. Fakeeha, A. H.; Bagabas, A. A.; Lanre, M. S.; Osman, A. I.; Kasim, S. O.; Ibrahim, A. A.; Arasheed, R.; Alkhalifa, A.; Elnour, A. Y.; Abasaeed, A. E.; Al-Fatesh, A. S., Catalytic Performance of Metal Oxides Promoted Nickel Catalysts Supported on Mesoporous γ-Alumina in Dry Reforming of Methane. *Processes* **2020,** *8* (5).

48. Castro Luna, A. E.; Iriarte, M. E., Carbon dioxide reforming of methane over a metal modified Ni-Al2O3 catalyst. *Applied Catalysis A: General* **2008,** *343* (1-2), 10-15.

49. Nandini, A.; Pant, K. K.; Dhingra, S. C., K-, CeO2-, and Mn-promoted Ni/Al2O3 catalysts for stable CO2 reforming of methane. *Applied Catalysis A: General* **2005,** *290* (1-2), 166-174.

50. Roh, H.-S.; Koo, K. Y.; Jeong, J. H.; Seo, Y. T.; Seo, D. J.; Seo, Y.-S.; Yoon, W. L.; Park, S. B., Combined reforming of methane over supported Ni catalysts. *Catalysis Letters* **2007,** *117* (1-2), 85-90.

51. Xu, L.; Song, H.; Chou, L., Carbon dioxide reforming of methane over ordered mesoporous NiO–MgO–Al2O3 composite oxides. *Applied Catalysis B: Environmental* **2011,** *108-109*, 177-190.

52. Özdemir, H.; Öksüzömer, M. A. F.; Gürkaynak, M. A., Effect of the calcination temperature on Ni/MgAl2O4 catalyst structure and catalytic properties for partial oxidation of methane. *Fuel* **2014,** *116*, 63-70.

53. Guo, Y.; Li, Y.; Ning, Y.; Liu, Q.; Tian, L.; Zhang, R.; Fu, Q.; Wang, Z.-j., CO2 Reforming of Methane over a Highly Dispersed Ni/Mg–Al–O Catalyst Prepared by a Facile and Green Method. *Industrial & Engineering Chemistry Research* **2020,** *59* (35), 15506-15514.

54. Wang, N.; Shen, K.; Huang, L.; Yu, X.; Qian, W.; Chu, W., Facile Route for Synthesizing Ordered Mesoporous Ni–Ce–Al Oxide Materials and Their Catalytic Performance for Methane Dry Reforming to Hydrogen and Syngas. *ACS Catalysis* **2013,** *3* (7), 1638-1651.

55. Tathod, A. P.; Hayek, N.; Shpasser, D.; Simakov, D. S. A.; Gazit, O. M., Mediating interaction strength between nickel and zirconia using a mixed oxide nanosheets interlayer for methane dry reforming. *Applied Catalysis B: Environmental* **2019,** *249*, 106-115.

56. Das, S.; Ashok, J.; Bian, Z.; Dewangan, N.; Wai, M. H.; Du, Y.; Borgna, A.; Hidajat, K.; Kawi, S., Silica–Ceria sandwiched Ni core–shell catalyst for low temperature dry reforming of biogas: Coke resistance and mechanistic insights. *Applied Catalysis B: Environmental* **2018,** *230*, 220-236.

57. Wei, J.; Iglesia, E., Isotopic and kinetic assessment of the mechanism of reactions of CH4 with CO2 or H2O to form synthesis gas and carbon on nickel catalysts. *Journal of Catalysis* **2004,** *224* (2), 370-383.

58. Yuan, K.; Zhong, J.-Q.; Zhou, X.; Xu, L.; Bergman, S. L.; Wu, K.; Xu, G. Q.; Bernasek, S. L.; Li, H. X.; Chen, W., Dynamic Oxygen on Surface: Catalytic Intermediate and Coking Barrier in the Modeled CO2 Reforming of CH4 on Ni (111). *ACS Catalysis* **2016,** *6* (7), 4330-4339.

59. Das, S.; Jangam, A.; Jayaprakash, S.; Xi, S.; Hidajat, K.; Tomishige, K.; Kawi, S., Role of lattice oxygen in methane activation on Ni-phyllosilicate@Ce1-xZrxO2 core-shell catalyst for methane dry reforming: Zr doping effect, mechanism, and kinetic study. *Applied Catalysis B: Environmental* **2021,** *290*.

60. Praserthdam, S.; Somdee, S.; Rittiruam, M.; Balbuena, P. B., Computational Study of the Evolution of Ni-Based Catalysts during the Dry Reforming of Methane. *Energy & Fuels* **2020,** *34* (4), 4855-4864.

61. Zhang, F.; Liu, Z.; Chen, X.; Rui, N.; Betancourt, L. E.; Lin, L.; Xu, W.; Sun, C.-j.; Abeykoon, A. M. M.; Rodriguez, J. A.; Teržan, J.; Lorber, K.; Djinović, P.; Senanayake, S. D., Effects of Zr Doping into Ceria for the Dry Reforming of Methane over Ni/CeZrO2 Catalysts: In Situ Studies with XRD, XAFS, and AP-XPS. *ACS Catalysis* **2020,** *10* (5), 3274-3284.

62. Bensalem, A.; Bozon-Verduraz, F.; Perrichon, V., Palladium–ceria catalysts: reversibility of hydrogen chemisorption and redox phenomena. *Journal of the Chemical Society, Faraday Transactions* **1995,** *91* (14), 2185-2189.

63. Lykhach, Y.; Staudt, T.; Vorokhta, M.; Skála, T.; Johánek, V.; Prince, K. C.; Matolín, V.; Libuda, J., Hydrogen spillover monitored by resonant photoemission spectroscopy. *Journal of Catalysis* **2012,** *285* (1), 6-9.

64. Karim, W.; Spreafico, C.; Kleibert, A.; Gobrecht, J.; VandeVondele, J.; Ekinci, Y.; van Bokhoven, J. A., Catalyst support effects on hydrogen spillover. *Nature* **2017,** *541* (7635), 68-71.

65. O'Brien, C. P.; Lee, I. C., Kinetic Modeling of Spillover and Temperature-Programmed Oxidation of Oxy-Carbon Surface Species on Pt/Al2O3. *The Journal of Physical Chemistry C* **2017,** *121* (22), 12329-12336.

66. Sarnello, E.; Lu, Z.; Seifert, S.; Winans, R. E.; Li, T., Design and Characterization of ALD-Based Overcoats for Supported Metal Nanoparticle Catalysts. *ACS Catalysis* **2021,** *11* (5), 2605-2619.

67. Suntola, T., Atomic layer epitaxy. *Materials Science Reports* **1989,** *4* (5), 261-312.

68. Leskelä, M.; Ritala, M., Atomic Layer Epitaxy in Deposition of Various Oxide and Nitride Thin Films. *J. Phys. IV France* **1995,** *05* (C5), C5-937-C5-951.

69. Ritala, M.; Leskelä, M.; Dekker, J.-P.; Mutsaers, C.; Soininen, P. J.; Skarp, J., Perfectly Conformal TiN and Al2O3 Films Deposited by Atomic Layer Deposition. *Chemical Vapor Deposition* **1999,** *5* (1), 7-9.

70. George, S. M.; Ott, A. W.; Klaus, J. W., Surface Chemistry for Atomic Layer Growth. *The Journal of Physical Chemistry* **1996,** *100* (31), 13121-13131.

71. George, S. M., Atomic Layer Deposition: An Overview. *Chemical Reviews* **2010,** *110* (1), 111-131.

72. Lu, Z.; Tracy, R. W.; Abrams, M. L.; Nicholls, N. L.; Barger, P. T.; Li, T.; Stair, P. C.; Dameron, A. A.; Nicholas, C. P.; Marshall, C. L., Atomic Layer Deposition Overcoating Improves Catalyst Selectivity and Longevity in Propane Dehydrogenation. *ACS Catalysis* **2020,** *10* (23), 13957-13967.

73. Gould, T. D.; Izar, A.; Weimer, A. W.; Falconer, J. L.; Medlin, J. W., Stabilizing Ni Catalysts by Molecular Layer Deposition for Harsh, Dry Reforming Conditions. *ACS Catalysis* **2014,** *4* (8), 2714-2717.

74. Ahn, S.; Littlewood, P.; Liu, Y.; Marks, T. J.; Stair, P. C., Stabilizing Supported Ni Catalysts for Dry Reforming of Methane by Combined La Doping and Al Overcoating Using Atomic Layer Deposition. *ACS Catalysis* **2022,** *12* (17), 10522-10530.

75. Margossian, T.; Larmier, K.; Kim, S. M.; Krumeich, F.; Fedorov, A.; Chen, P.; Muller, C. R.; Coperet, C., Molecularly Tailored Nickel Precursor and Support Yield a Stable Methane Dry Reforming Catalyst with Superior Metal Utilization. *J Am Chem Soc* **2017,** *139* (20), 6919-6927.

76. Ingale, P.; Guan, C.; Kraehnert, R.; Naumann d'Alnoncourt, R.; Thomas, A.; Rosowski, F., Design of an active and stable catalyst for dry reforming of methane via molecular layer deposition. *Catalysis Today* **2021,** *362*, 47-54.

77. Afzal, S.; Prakash, A. V.; Littlewood, P.; Marks, T. J.; Weitz, E.; Stair, P. C.; Elbashir, N. O., Controlling the rate of change of Ni dispersion in commercial catalyst by ALD overcoat during dry reforming of methane. *International Journal of Hydrogen Energy* **2020,** *45* (23), 12835-12848.

78. Jiang, C.; Loisel, E.; Cullen, D. A.; Dorman, J. A.; Dooley, K. M., On the enhanced sulfur and coking tolerance of Ni-Co-rare earth oxide catalysts for the dry reforming of methane. *Journal of Catalysis* **2021,** *393*, 215-229.

79. Aireddy, D. R.; Yu, H.; Cullen, D. A.; Ding, K., Elucidating the Roles of Amorphous Alumina Overcoat in Palladium-Catalyzed Selective Hydrogenation. *ACS Appl Mater Interfaces* **2022,** *14* (21), 24290-24298.

80. Varez, A.; Garcia-Gonzalez, E.; Jolly, J.; Sanz, J., Structural characterization of Ce1−xZrxO2 ($0 \leq x \leq 1$) samples prepared at 1650°C by solid state reaction: A combined TEM and XRD study. *Journal of the European Ceramic Society* **2007,** *27* (13), 3677-3682.

81. George, C.; Littlewood, P.; Stair, P. C., Understanding Pore Formation in ALD Alumina Overcoats. *ACS Appl Mater Interfaces* **2020,** *12* (18), 20331-20343.

82. Aspen Technology, I. *Aspen HYSYS V12*, Aspen Technology, Inc.: 2020.

83. Reddy, B. M.; Thrimurthulu, G.; Katta, L., Design of Efficient CexM1−xO2−δ (M = Zr, Hf, Tb and Pr) Nanosized Model Solid Solutions for CO Oxidation. *Catalysis Letters* **2010,** *141* (4), 572-581.

84. Hu, Z.; Liu, X.; Meng, D.; Guo, Y.; Guo, Y.; Lu, G., Effect of Ceria Crystal Plane on the Physicochemical and Catalytic Properties of Pd/Ceria for CO and Propane Oxidation. *ACS Catalysis* **2016,** *6* (4), 2265-2279.

85. Papaefthimiou, V.; Niakolas, D. K.; Paloukis, F.; Dintzer, T.; Zafeiratos, S., Is Steam an Oxidant or a Reductant for Nickel/Doped-Ceria Cermets? *Chemphyschem* **2017,** *18* (1), 164-170.

86. Mullins, D. R.; Overbury, S. H.; Huntley, D. R., Electron spectroscopy of single crystal and polycrystalline cerium oxide surfaces. *Surface Science* **1998,** *409* (2), 307-319.

87. Wang, J.; Shen, M.; Wang, J.; Yang, M.; Wang, W.; Ma, J.; Jia, L., Effects of Ni-Doping of Ceria-Based Materials on Their Micro-Structures and Dynamic Oxygen Storage and Release Behaviors. *Catalysis Letters* **2010,** *140* (1-2), 38-48.

88. Ivanova, A. S., Physicochemical and catalytic properties of systems based on CeO2. *Kinetics and Catalysis* **2009,** *50* (6), 797-815.

89. O'Quinn, E. C.; Shamblin, J.; Perlov, B.; Ewing, R. C.; Neuefeind, J.; Feygenson, M.; Gussev, I.; Lang, M., Inversion in Mg1–xNixAl2O4 Spinel: New Insight into Local Structure. *Journal of the American Chemical Society* **2017,** *139* (30), 10395-10402.

90. Wyckoff, R. W. G., The X-Ray Scattering Powers of Nickel and Oxygen in Nickel Oxide. *Physical Review* **1930,** *35* (6), 583-587.

91. Smrcok, L.; Langer, V.; Krestan, J., [gamma]-Alumina: a single-crystal X-ray diffraction study. *Acta Crystallographica Section C* **2006,** *62* (9), i83-i84.

92. Artini, C.; Pani, M.; Carnasciali, M. M.; Buscaglia, M. T.; Plaisier, J. R.; Costa, G. A., Structural features of Sm- and Gd-doped ceria studied by synchrotron X-ray diffraction and mu-Raman spectroscopy. *Inorg Chem* **2015,** *54* (8), 4126-37.

93. Giehr, A.; Maier, L.; Schunk, S. A.; Deutschmann, O., Thermodynamic Considerations on the Oxidation State of Co/γ-Al2O3 and Ni/γ-Al2O3 Catalysts under Dry and Steam Reforming Conditions. *ChemCatChem* **2018,** *10* (4), 751-757.

94. Shan, W.; Fleys, M.; Lapicque, F.; Swierczynski, D.; Kiennemann, A.; Simon, Y.; Marquaire, P.-M., Syngas production from partial oxidation of methane over Ce1−XNiXOY catalysts prepared by complexation–combustion method. *Applied Catalysis A: General* **2006,** *311*, 24-33.

95. Shyu, J. Z.; Weber, W. H.; Gandhi, H. S., Surface characterization of alumina-supported ceria. *The Journal of Physical Chemistry* **1988,** *92* (17), 4964-4970.

96. Martínez-Arias, A.; Fernández-García, M.; Salamanca, L. N.; Valenzuela, R. X.; Conesa, J. C.; Soria, J., Structural and Redox Properties of Ceria in Alumina-Supported Ceria Catalyst Supports. *The Journal of Physical Chemistry B* **2000,** *104* (17), 4038-4046.

97. Han, B.; Zhao, L.; Wang, F.; Xu, L.; Yu, H.; Cui, Y.; Zhang, J.; Shi, W., Effect of Calcination Temperature on the Performance of the Ni@SiO2 Catalyst in Methane Dry Reforming. *Industrial & Engineering Chemistry Research* **2020,** *59* (30), 13370-13379.

Vita

Education

Master of Science, Cain Department of Chemical Engineering, Louisiana State University, Baton Rouge, LA. Master's Thesis: *Improved Selectivity and Stability in Methane Dry Reforming by Atomic Layer Deposition onto Ni-CeO_2-ZrO_2/Al_2O_3 Catalysts.* Advisor: Professor Kerry Dooley. May 2023

Bachelor of Science, Chemical Engineering, Louisiana State University, Baton Rouge, LA. May 2020.

Publications and Presentations

Lucas, J., Airreddy, D., Ding, K., Roy, A., Cullen, D., Dorman, J.A, Dooley, K., "Improved Selectivity and Stability in Methane Dry Reforming by Atomic Layer Deposition onto Ni-CeO_2-ZrO_2/Al_2O_3 Catalysts "Abstract for the 28th annual North American Catalysis society Meeting Summer 2023, Providence, Rhode Island (2023)

Lucas, J., Roman, C., Airreddy, D., Ding, K., Roy, A., Cullen, D., Dorman, J.A., Dooley, K, "Improved Selectivity and Stability in Methane Dry Reforming by Atomic Layer Deposition onto Ni-CeO_2-ZrO_2/Al_2O_3 Catalysts ". Post presentation at the American Institution of Chemical Engineers Fall 2022 Annual Meeting, Pheonix Arizona (2022).

Lucas, J., Airreddy, D., Ding, K., Roy, A., Cullen, D., Dooley, K., Dorman, J.A., "Importance of Precise Nickel Siting and Dispersion in Supported Nickel Dry Reforming Catalysts". Post presentation at the 27th annual North American Catalysis Society Meeting Summer 2022, New York, New York (2022).

I would like to thank everyone who helped me with this Masters degree: my family, friends, Dr. Dorman, Dr. Dooley, and all my fellow lab members. I have enjoyed this quest for knowledge, and I hope I get the opportunity to continue. I anticipate receiving my M.S in Chemical Engineering in May of 2023